Development and Testing of *Operando* Degradation Protocols for Perovskite Solar Cells Using Grazing Incidence Wide Angle X-ray Scattering

A Thesis Submitted to the College of

Graduate and Postdoctoral Studies

in Partial Fulfillment of the Requirements

for the Degree of Masters of Science

in the Department of Chemistry

University of Saskatchewan

Saskatoon

By

Kyle M. Fransishyn

Permission to Use

In presenting this thesis/dissertation in partial fulfillment of the requirements for a Postgraduate degree from the University of Saskatchewan, I agree that the Libraries of this University may make it freely available for inspection. I further agree that permission for copying of this thesis/dissertation in any manner, in whole or in part, for scholarly purposes may be granted by the professor or professors who supervised my thesis/dissertation work or, in their absence, by the Head of the Department or the Dean of the College in which my thesis work was done. It is understood that any copying or publication or use of this thesis/dissertation or parts thereof for financial gain shall not be allowed without my written permission. It is also understood that due recognition shall be given to me and to the University of Saskatchewan in any scholarly use which may be made of any material in my thesis.

Requests for permission to copy or to make other uses of materials in this thesis/dissertation in whole or part should be addressed to:

Dean
College of Graduate and Postdoctoral Studies
University of Saskatchewan
116 Thorvaldson Building, 110 Science Place
Saskatoon, Saskatchewan S7N 5C9
Canada

Department Head
Department of Chemistry
University of Saskatchewan
110 Science Place
Saskatoon, Saskatchewan S7N 5C9
Canada

Abstract

Solar cells based on lead halide perovskites recently made large improvements to device power conversion efficiency through active layer design and device engineering. However, current best practices for improving device performance focus on engineering-based solutions such as encapsulation to try and stabilize devices. The improvement in intrinsic device stability for higher yielding perovskite solar cells has only made marginal gains for commercial application. The goal of making an intrinsically stable solar cell requires a fundamental understanding of the different degradation pathways with a way to measure devices to determine which pathway or combination of pathways causes device failure. Here I design an experimental protocol that can measure performance and structural characteristics of perovskite solar cells in an environmentally controlled chamber. These experiments test full devices while an X-ray beam from a synchrotron source probes the device for structural information. Under different experimental conditions the device degradation is a complex combination of different degradation and healing mechanisms. The main influencing factor in device failure can vary across different measurement protocols and within the same protocols due to minor differences in layer deposition and from defects present within the films. Due to how changes in the experimental environment affects device performance the correlation of data between different measurements is problematic. Therefore, the measurements are gathered simultaneously to increase the accuracy of correlations made between separate data sets. The goal of this thesis is show the preparation and application of an *operando* chamber at the Canadian Light Source and the analysis of the time resolved correlated data that can be acquired from this experimental setup.

Co-Authorship Statement

Unless otherwise noted, I preformed all experimental work, data analysis, and wrote the first draft of the manuscript. S. Kundu developed the process for fabrication of the perovskite solar cells and contributed in manufacturing the samples used. S. Kundu and K. Poorkazem assisted in data collection at the Canadian Light Source for the grazing incidence wide angle X-ray scattering experiments. T. L. Kelly supervised the development of the device fabrication, manufacturing, and testing as well as the chamber fabrication and o*perando* studies in conjunction with providing research guidance and revising the manuscript.

Acknowledgements

First, I would like to thank Dr. Timothy L. Kelly for the opportunity to work in his lab group and the academic support he as given. He has kept me on track by pulling me out of the weeds when I went off on tangents and kept me motivated to keep pushing through when things got bogged down and felt like nothing was progressing. Thank you for helping me accomplish this achievement in my life.

The friends and colleagues that I met in the Kelly group have been and continue to be supportive in my academic and personal life. I specifically want to thank Nick Randell who supervised my undergrad project, without him and Dr. Kelly I would have never continued to graduate school; I hold them responsible for the experiences I have gained.

I wish to thank the Dr. George Belev who I worked under at BMIT at the Canadian Light Source, he sparked my curiosity about X-rays and synchrotrons. Without him and the staff at BMIT I would not have had the practical knowledge that allowed me to approach the problems of my project.

I would also like to thank Dr. Thomas Ellis from my advisory committee for giving me advice and support throughout my writing process and keeping me on track.

Finally, I want to thank my family who have supported and encouraged me through my academic career. I would not be the person I am today without their love and support.

Table of Contents

List of Figures

List of Abbreviations

CB	Conduction band
CBM	Conduction band minimum
CCD	Charge capture device
CLS	Canadian Light Source
ETL	Electron transport layer
FA	Formamidinium
FF	Fill factor
FTO	Fluorine doped tin oxide
GIWAXS	Grazing incidence wide angle X-ray scattering
HTL	Hole transport layer
HXMA	Hard X-ray MicroAnalysis
I_{sc}	Short circuit current
ITO	Indium tin oxide
I-V	Current-voltage
LED	Light emitting diode
MA	Methylammonium
$MAPbI_3$	Methylammonium lead iodide
MFC	Mass flor controller
P3HT	Poly-(3-hexylthiophene)
PCE	Power conversion efficiency
PV	Photovoltaics
pXRD	Powder X-ray diffraction

RH	Relative humidity
R_S	Series resistance
R_{Sh}	Shunt resistance
SEM	Scanning electron microscopy
Spiro-OMeTAD	2,2',7,7'-Tetrakis[N,N-di(4-methoxyphenyl)amino]-9,9'-spirobifluorene
TCO	Transparent conductive oxide
VB	Valence band
VBM	Valence band maximum
V_{oc}	Open circuit voltage
XRD	X-ray diffraction

Chapter 1 Introduction

1.1 Solar Energy

Global climate change is becoming a larger influence on global policy , and is even starting to impact local policy.[1,2] The demand for alternative energy sources, such as solar energy, wind, tidal, and hydro-electric is increasing. At the same time, the cost per-kilowatt hour for solar energy is now lower than many traditional energy sources, such as coal and nuclear.[3] To maintain this price advantage through the increase in demand, we require renewable technologies that can scale to the current and future electrical demand of society. Solar cell technology provides a reasonable alternative to non-renewables as part of the overall solution for the world's energy needs. For solar cells to remain a competitive technology, methods of increasing manufacturing output and increasing power conversion efficiency (PCE) will need to be developed.

The main commercial technologies for solar cells are silicon-based photovoltaics (PV), gallium arsenide (GaAs) PV, and cadmium telluride (CdTe) PV. The current efficiency records for lab-scale cells are shown in Figure 1.1 . Currently, multi-crystalline silicon cells have the largest market share of commercially produced solar cells, whereas monolithic (single crystal) silicon solar cells have higher PCE. Silicon currently produces 26.6%[4] efficient cells (non-concentrator) in the lab. The maximum limit of the material, based on the Shockley–Queisser limit[5,6] and the band gap of silicon (1.1 eV), is 32.2%.Although multi-crystalline silicon cells are much easier to manufacture than the single crystal version, they both still require highly purified starting material and are intrinsically rigid and inflexible. To push solar cell manufacturing

towards higher output, we need solar cell technology that is compatible with high throughput manufacturing methods, such as roll-to-roll processing.

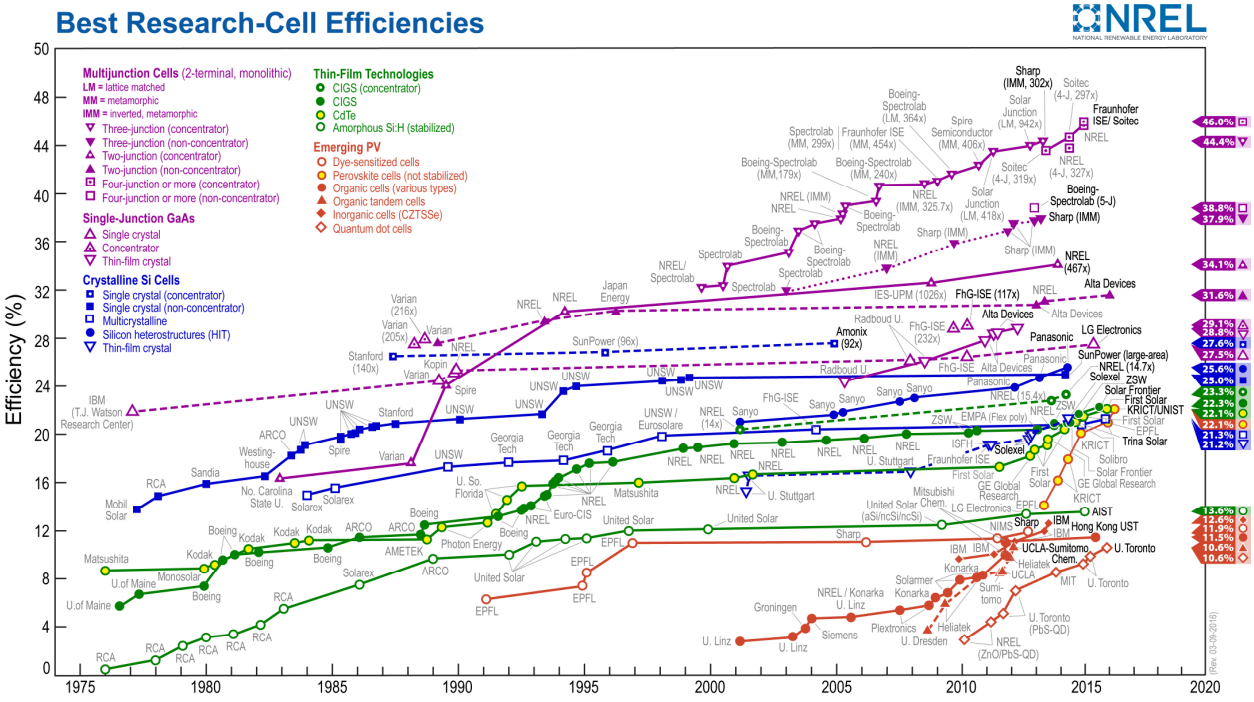

Figure 1.1 Record-setting solar cell efficiencies. Figure reproduced from reference.[4]

GaAs devices have a better band gap for matching the spectral output of the sun. GaAs is epitaxially grown to produce these cells, and is generally extremely expensive to produce. GaAs is also not as air stable when compared to silicon. The main application for this technology is in satellites, where the cost is not as important as the power-to-weight ratio. With a record efficiency of 28.8%,[7] a higher efficiency means fewer panels for an equivalent power output, and operating in a vacuum environment reduces concerns about air stability. The Shockley–Queisser limit for GaAs (based on a band gap of 1.4 eV) is 32.9%.

The other main commercial technology for solar cells available is CdTe thin film devices. These devices are thin film based, rather then fully crystalline. This means that devices are made

without the requirement of growing large, near perfect crystals, and have a lower manufacturing cost. However, the downsides are their lower efficiencies (record of 22.1%[7]), and the high toxicity of the cadmium salts. While the risk of exposure to toxic elements can be minimized by properly recycling the cells after use and using best practices, for manufacturing their risks present a significant draw back to the technology. The Shockley–Queisser limit for CdTe (based on a band gap of 1.5 eV) is 31.6%.

Some of these technologies are approaching the Shockley-Queisser limit. A way to get around this limit is to increase the complexity of the cells and produce multi-junction solar cells,[8–11] which often use concentrators.[12,13] The increased complexity of these multi-junction cells make them prohibitively expensive to manufacture. They require materials that can be deposited on one another and have an absorbance profile that is offset from material underneath it and remains transparent to wavelengths the material absorbs at.

Thin film solar cells that are intrinsically flexible and solution processable can take advantage of higher throughput methods such as printing and roll-to-roll manufacturing.[14–18] They can also be used in conjunction with current silicon technology to produce multi-junction solar cells,[9,11]since they can be cast onto silicon. There are a range of thin film technologies, such as organic photovoltaics,[8,19,20] quantum dots,[21–23] and perovskites,[24–26] that can be tuned to work either as independent devices, or in conjunction with silicon solar cells. One of the most promising technologies are perovskite based solar cells, as they have shown a rapid increase in PCE from their initial performance of 3.8% in 2009[27] to a current certified efficiency of 22.1% in 2017.[28]

1.2 Perovskite Solar Cells

Perovskite is a type of crystal structure based on the mineral calcium titanite ($CaTiO_3$). Perovskites have a formula of ABX_3, where A and B are different sized cations and X is an anion that balances the charge. In solar cell applications, perovskites typically refer to a specific class of materials were A is an organic or inorganic cation, B is a divalent metal (Pb^{2+}, Sn^{2+}),[25,27,29,30] and X is a halide (Cl^-, Br^-, I^-).[30–33]

The reason for the growing interest in perovskite-based devices is the rapid increase in device performance over the past decade. They are also easily made through simple solution processes. This means that the technology can take advantage of manufacturing processes such as slot die coating, ink jet printing, and blade coating. These films are mostly polycrystalline, and have more flexibility than monolithic structures, making them compatible with roll-to-roll processing.[34–39] However, the main disadvantage of perovskite solar cells is their lack of stability in different environments (water, oxygen).[40–44] Researchers are attempting to find new perovskite compositions to improve stability, and develop new device architectures to improve device lifetimes. This thesis deals with the stability and lifetimes of perovskite solar cells based on methylammonium lead iodide ($MAPbI_3$).

1.2.1. Crystal Structure

The crystal structure of $MAPbI_3$ is shown in Figure 1.2. $MAPbI_3$ adopts a tetragonal structure at room temperature. The lead and iodine atoms form an octahedral coordination geometry that makes up the bulk lattice structure. The methylammonium (MA) ions occupy the open holes between lead-iodide octahedral units in the lattice. The hydrogen bonding between the N-H and I group account for the distortions from cubic symmetry. An increase in the

temperature causes an increase in the orientational motion of the MA, weakening the N-H---I bonding; a decrease in the temperature has the opposite effect. The strength of N-H---I bonding at different temperatures is what induces different phase changes: orthorhombic to tetragonal at 165 K and tetragonal to cubic at 327 K. The orthorhombic and cubic structures are shown in Figure 1.3.

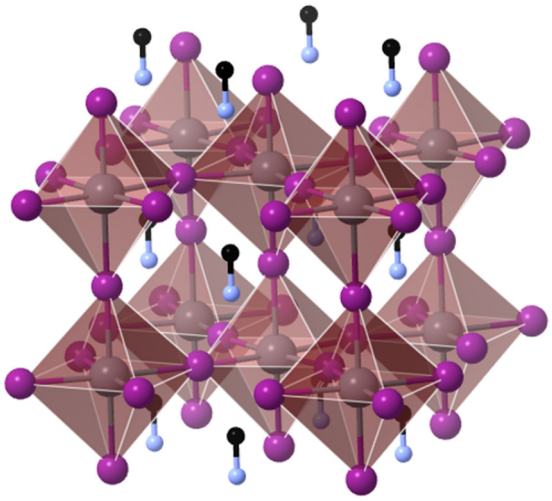

Figure 1.2 Structure of $MAPbI_3$ in the tetragonal phase.

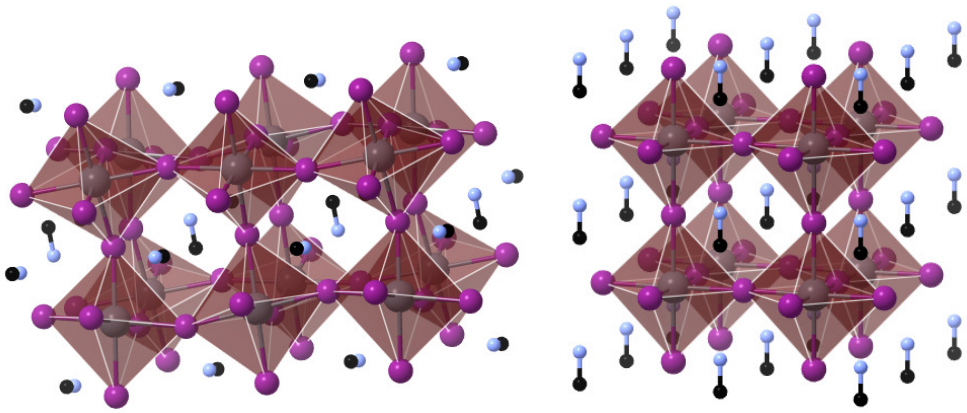

Figure 1.3 Structure of orthorhombic (left) and cubic (right) $MAPbI_3$.

The different phases of $MAPbI_3$ are all direct band gap semiconductors with similar band gaps. However, the effect that the phase has on the hysteresis of the solar cell can be different and will be discussed in section 1.2.3. The focus of this thesis will be $MAPbI_3$ perovskite films in the tetragonal phase.

The main way to characterize these perovskite films and determine their phase purity is to perform powder X-ray diffraction. The calculated diffraction pattern shown in Figure 1.4 shows the peaks that would be expected for $MAPbI_3$ analyzed with a 0.6888 $Å^{-1}$ source. The main diagnostic peak used to measure the quality of the perovskite films is the (110) reflection. The other major reflections are also labeled in Figure 1.4; the smaller intensity reflections that are not labeled are not usually resolvable due to the width of neighbouring peaks.

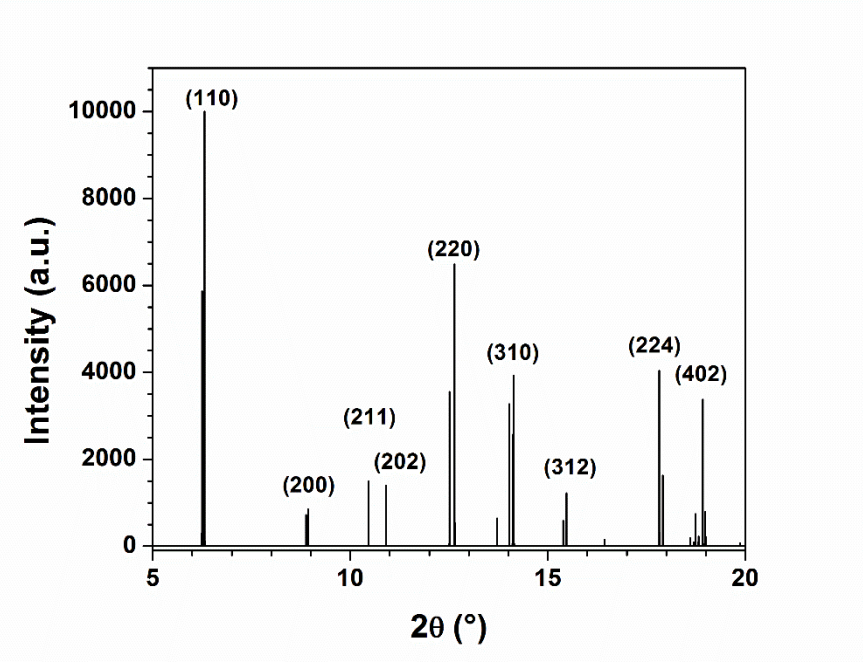

Figure 1.4 Simulated diffraction pattern of $MAPbI_3$ with a 0.6888 $Å^{-1}$ source and major peak assignments.

1.2.2. Device Principles

A perovskite solar cell takes on the general form shown in Figure 1.5 with each different layer playing an important part in the function of the solar cell. The active layer in the solar cell is the perovskite material which absorbs a photon of light and excites an electron from the valence band into the conduction band, as shown in Figure 1.6. The valence band maximum (VBM) being the highest orbital energy that contains electrons, with the conduction band minimum (CBM) being the lowest orbital band that is empty of any electrons. The difference in energy between the VBM and the CBM is the band gap of the material.

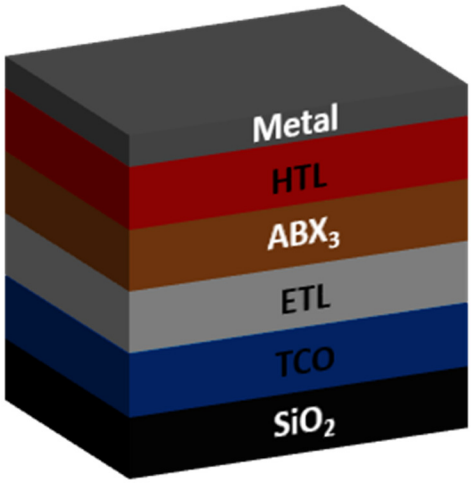

Figure 1.5 General structure of a perovskite device.

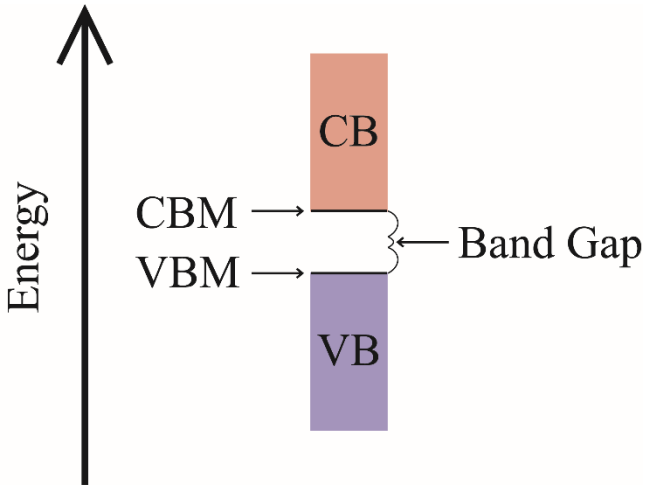

Figure 1.6 Outline of a band structure; conduction band (CB) and valence band (VB).

The band gap energy is the lowest energy of light that can be absorbed by the material. This onset of absorption can be seen in the UV/Vis spectrum of the material (Figure 1.7). The absorption of light beyond the onset of absorption is due to the density of states of filled/empty electron orbitals that lie within the VB/CB of the material.

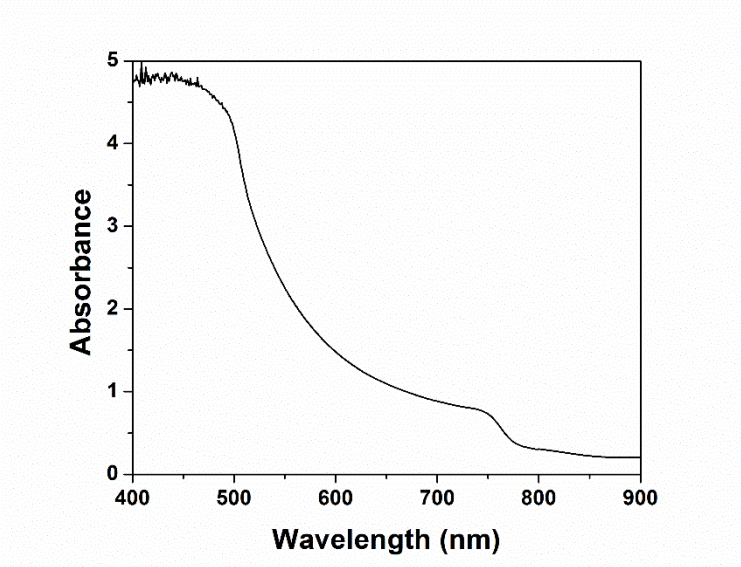

Figure 1.7 UV/Vis spectrum of a $MAPbI_3$ thin film on TiO_2 and glass.

Once the material absorbs a photon of light, it creates an electron-hole pair in the material (called an exciton), which can be broken down into two categories. The first type is the Frenkel exciton which exists in low dielectric constant materials and has a higher binding energy, on the order of 0.1 - 1.0 eV. This means that the electron-hole pair is very tightly bound together, and this coulombic interaction must be broken to separate them into free charge carriers. The other type of exciton is the Wannier-Mott exciton; these exist in materials with larger dielectric constants and have lower coulombic interaction between the electron and hole pair. This lower interaction means the electron-hole pair is much more spaced out in the material, with the binding energy being as low as 0.01 eV. In work done by Snaith *et al.*[45] it was shown that the binding energy of an exciton in a $MAPbI_3$ thin film is 0.050 ± 0.020 eV; the charge carriers can drift up to ~2.3 nm[46] from each other. This means that the excitons generated in the film are Wannier-Mott excitons and can undergo much easier charge separation.

Charge separation is an important process in solar cells since excitons have a finite lifetime, after which the excited electron recombines with the hole. To have efficient charge

separation, the devices require interfaces that selectively transport only one type of charge carrier. These are the interlayers on either side of the active layer; here the electron transport layer is at the bottom and the hole transport layer is at the top. The orbitals of these materials need to have energies such that they can effectively only extract a specific charge carrier. The electron transport layer (ETL) allows the extraction of electrons and the hole transport layer (HTL) extracts holes from the perovskite, seen in Figure 1.8.

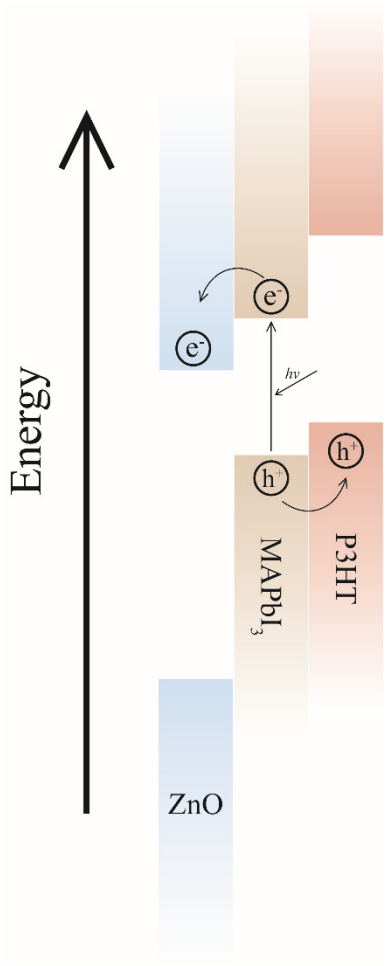

Figure 1.8 Hole and electron extraction from $MAPbI_3$ by interlayers.

The ETL interlayer can be made from materials such as TiO_2 or ZnO. The active layer of the device is made from the perovskite material (ABX_3), and is where photocurrent is generated in the device. The final interlayer is the HTL, which is made from materials such as poly-(3-

hexylthiophene) (P3HT) or 2,2',7,7'-Tetrakis[N,N-di(4-methoxyphenyl)amino]-9,9'-spirobifluorene (Spiro-OMeTAD). The device is then capped with electrodes made from a metal such as gold or silver on top of the HTL. The ETL is on the substrate which is made from glass that has a coating of a transparent conductive oxide (TCO). The TCO is usually made from indium tin oxide (ITO) or fluorine doped tin oxide (FTO). The TCO forms the other electrode for the device and is the substrate that the device is built upon.

While interlayers help with charge extraction and improve device performance, they also increase device complexity, necessitating more optimization. Two key diagnostic factors in device optimization are the parasitic resistances. Two types of resistance are determined for devices: series and shunt resistance, as shown in Figure 1.9. For a solar cell the series resistance is desired to be as low as possible, as it impedes charge flow through the device. Series resistance can be caused by materials that have lower conductivity (either due to their inherent properties or the presence of impurities), delamination or gaps in the layers due to poor adhesion, manufacturing defects, and degradation. For shunt resistance, the device is shorted in a way that bypasses the active layer and charge leaks through the device. For an ideal device, the shunt resistance should be very high. A low shunt resistance is usually caused by defects in the active layer that causes the anode and cathode of the device to short together. In the processing stage pinholes can form in the film leading to a decrease in the shunt resistance. During degradation, defects can be created in the film that reduces the shunt resistance; in cases of full failure, the whole device short circuits, resulting in no power being generated.

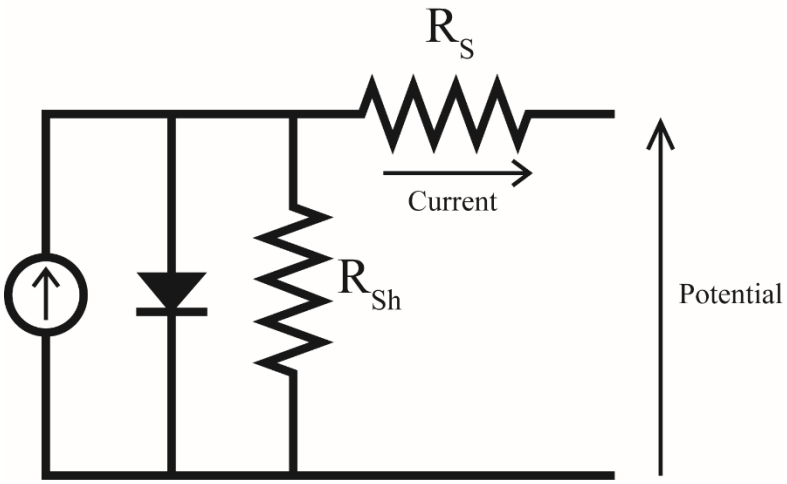

Figure 1.9 Equivalent circuit model of a solar cell, including the series (R_S) and shunt (R_{Sh}) resistance.

1.2.3. Device Electrical Data Analysis and Processing

The electrical data gathered from the devices consists of current-voltage (I-V) curves acquired using a source-measure unit. In Figure 1.10, I-V curves for both as-prepared and degraded devices are shown. From the graph, the change in open circuit voltage (V_{oc}) and short circuit current (I_{sc}) can be seen. The V_{oc} is the x-intercept in the graph, and the I_{sc} is the y-intercept of the graph. This tells us the maximum operating voltage and maximum current output of the device. The V_{oc} is characteristic of the band gap and band mismatch of the layers in the device. Information about the series resistance can also be obtained from the slope in this region of the graph. The I_{sc} is characteristic of how many charge carriers can be extracted from the device. From this region the inverse of the slope approximates the shunt resistance of the device.

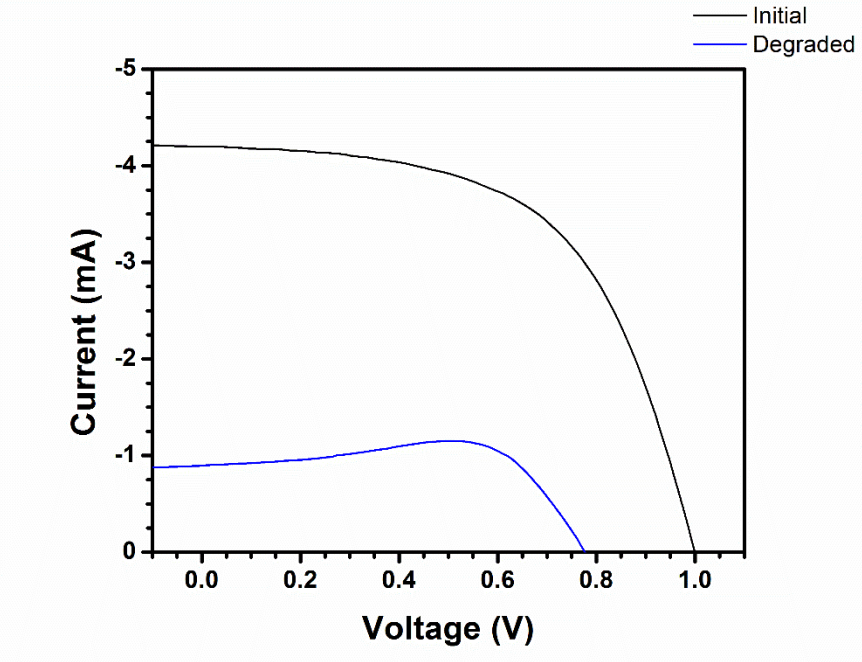

Figure 1.10 I-V curves of as prepared (black line) and degraded (blue line) solar cells.

The PCE is determined by the maximum power output of the device along the I-V curve. The power is determined by multiplying the voltage by the current along the curve, as shown in Figure 1.11. The maximum power output is divided by the incident power to determine the PCE. By comparing the area of the maximum power point (shown as the grey square) to the area of an ideal device (shown as the red square) we can calculate the fill factor (FF). The FF is an ideality measurement of the device compared to the V_{oc} and I_{sc}. The FF and PCE is affected by everything that affects I_{sc} and V_{oc}, and it is also affected by the hysteresis inside the sample. Hysteresis is due to temporary charge build up in a device as an electrical field is applied to it. As the voltage is swept, the device discharges, giving rise to a temporarily higher current output. The extreme of this effect can be seen in Figure 1.10 in the I-V curve of the degraded device. The device shows a bump-like structure at the maximum power point. This gives rise to a higher PCE and FF than what the device would show in a steady state measurement.

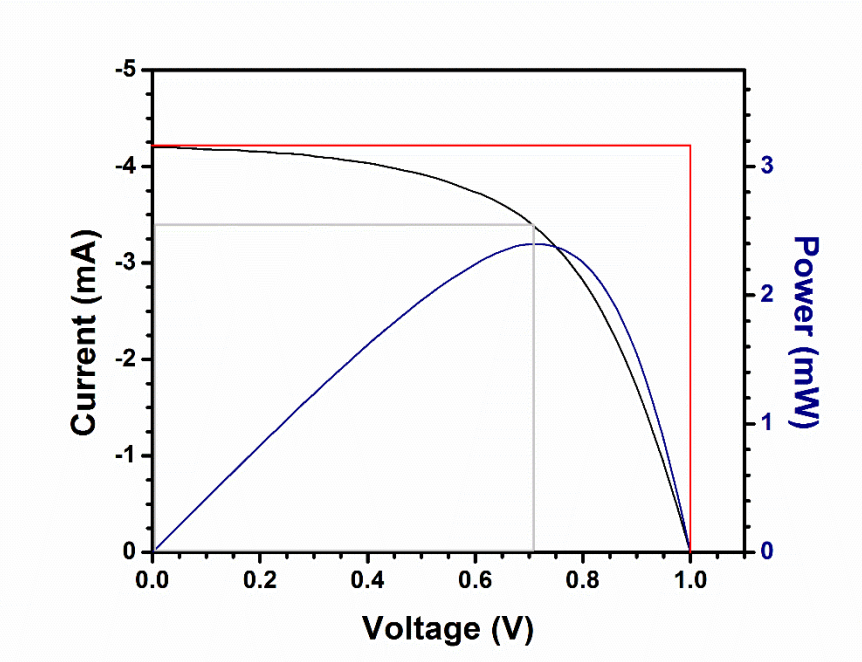

Figure 1.11 I-V curve of device (black line) with power output (blue line) and ideal device (red line) with actual device (grey line).

The data from these measurements can be plotted against time, as shown in Figure 1.12. The plot allows the device parameters to be viewed over time, to see how the device properties change in response to environmental stimuli. These parameters will later be compared to the X-ray diffraction data to see how trends in the crystal structure compare to device trends. All device data in this form is normalized to the first scan. The reason for normalization is that due to device to device variation, direct comparisons between absolute device parameters is difficult. Only trends in devices compared to the starting state is what is compared between devices.

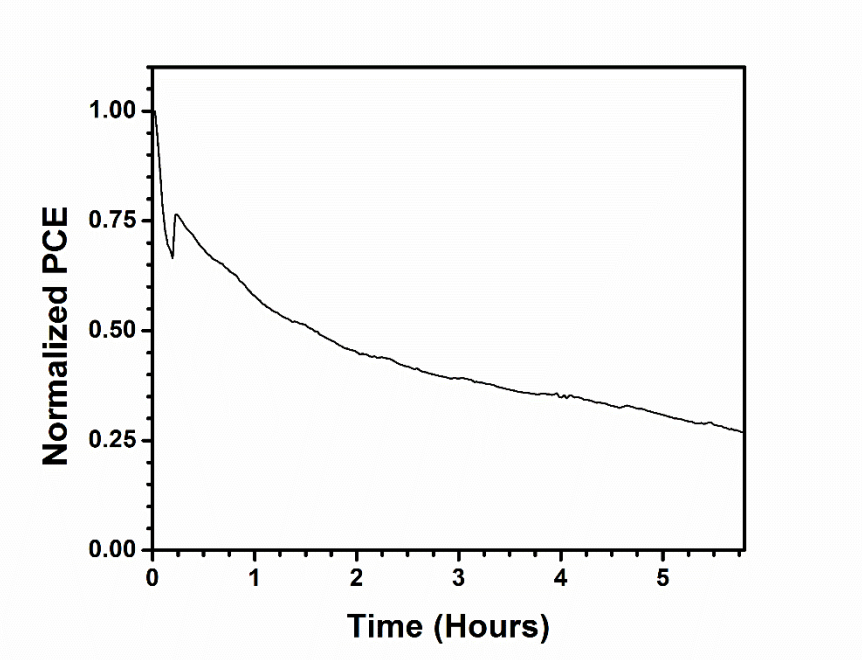

Figure 1.12 PCE versus time for a device in +85% RH.

1.2.4. Evolution of Perovskites to Current state-of -the-Art

In 2009, lead halide perovskites were used for the first time in a solar cell. The cells used a liquid analyte to shuttle holes to the counter electrode and produced 3.8% device efficiencies.[27] However, the perovskite was not stable in the liquid and degraded rapidly. In 2012 Snaith *et al.*[47] used a solid-state material (Spiro-OMeTAD) as the hole transport layer, and produced a device with near 8% PCE. The cell used a compact/ mesoporous TiO_2 electron transport layer with $MAPbI_3$ active layer and Spiro-OMeTAD as the hole transport layer.

Research into perovskite solar cells was originally focused on producing higher efficiency devices[48,49] by improving deposition methods and by changing the active material composition. Different ETL were also studied, as TiO_2 requires sintering at 450 °C, which is not suitable for either ITO or flexible substrates. Two possible candidates were Al_2O_3[47] and ZnO.[35] Al_2O_3 is an insulating material and showed that a mesoporous layer is only need as a scaffold,

and not for charge transport. ZnO was used in planar heterojunction devices and could be spin coated from solution without sintering; unfortunately ZnO produces thermally unstable devices with $MAPbI_3$.[41]

Initially the highest performing perovskites used methylammonium as the cation and iodine as the anion; $MAPbI_3$ produces cells with power conversion efficiencies as high as 19.7%.[32] However, they are highly unstable towards multiple different environments such as moisture,[40,50,51] oxygen,[42] and heat.[41,52] This will be further discussed in Section 1.3. These devices have two types of ETL configurations: compact and mesoporous. The mesoporous TiO_2 scaffolding has been shown to improve stability;[53] in this thesis, ZnO planar heterojunction based solar cells will be discussed.

Previous research has shown that the halide anion can tune the band gap of the perovskite material.[54,55] There can also be some tuning via the A site cation in the material.[49,56] This leads to the formation of mixed perovskite materials. By combining these materials, the material can be engineered to have a more optimal band gap. An example of a mixed perovskite material takes on the form $FA_yMA_{1-y}PbBr_xI_{3-x}$.[26,28] The combined Br^- and I^- gives a better band gap and increases the thermal stability of the material. The mixture of A site cations can be optimized to produce a high efficiency and increase of stability. The increase in stability is due to the reduced amount of MA that is present. MA is one of the main causes of the instability towards moisture, due to the acidic proton on the nitrogen. In formamidinium (FA) the acidic proton in stabilized through resonance. The combination of FA and MA can lead to phase separated domains that reduce the efficiency of the device, so a small amount of Cs^+ is often added to keep the proper structure and improve stability.[57] The highest performing devices now use a mixed perovskite

composition; through templating and process control, efficiencies of over 22% have been reported.[26,28]

1.3 Device and Active Layer Stability

1.3.1. Effects of Humidity on $MAPbI_3$

With improved device efficiency, short device lifetime is now the most significant hurdle for the commercialization perovskite solar cells. The degradation pathway for the $MAPbI_3$ is a reversible hydration process as water penetrates the crystal structure. The penetration is due to the polar water molecule being attracted to the A site cation. As the water penetrates the structure it causes strain on the surrounding framework and causes the crystal structure to adopt a new form. As shown in Equation 1, initial hydration of the perovskite distorts the crystal structure to first form a hydrate phase, which is the first intermediate degradation product. The formation of hydrate (1) is reversible as the water molecule can leave the perovskite, reverting it back to the original structure. The formation of the second hydrate (2) not only affects the crystal structure, it also produces the degradation product PbI_2 in the active layer.[58]

Equation 1 Hydrate formation

$$MAPbI_3 + H_2O \rightleftharpoons MAPbI_3 \bullet H_2O \quad (1)$$

$$4\,MAPbI_3 + H_2O \rightleftharpoons MA_4PbI_6 \bullet 2H_2O + 3\,PbI_2 \quad (2)$$

The monohydrate that reversibly forms with prolonged exposure to humidity breaks down into the starting materials PbI_2, methylamine gas (CH_2NH_2) and hydroiodic acid (HI). The methylamine gas is liberated from the sample and cannot react with the PbI_2 and HI to reform the perovskite structure. This leaves behind the degradation materials PbI_2 and HI in the sample. The

PbI_2 forms a crystalline solid that can be monitored with the use of X-ray diffraction. This process can also happen without going through the hydrate phase[58] and is shown in Equation 2.

Equation 2 Direct degradation

$$MAPbI_3 \longrightarrow PbI_2 + MAI \quad \text{or } (CH_2NH_2 \text{ and } HI)$$

Even though humidity is shown to be quite detrimental to the $MAPbI_3$ material, in small quantities it can have a healing effect. This healing effect is caused by the reversible nature of the degradation process. If only a small amount of humidity is present, the material can dissolve and reform at the grain boundaries recovering or increasing the crystallinity of the sample and forming larger grains. This process can be taken advantage of in the process of making perovskite films to try and improve the quality of the perovskite formed. This has shown some success in the literature to improve device performance.[59] However, current best practices have moved away from using this method as other approaches have been developed to form perovskites films with large grains and smooth surfaces.

1.3.2. Thermal and Oxygen Decomposition of Perovskite Active Layer

The effect of humidity on perovskites was discussed in 1.3.1; however, there are other pathways which are of concern in perovskite devices. One of the main concerns for perovskites is thermal stability, as commercial solar cells can reach temperatures as high as 85 °C in extreme conditions. Initial research showed that perovskites would not chemically break down until 473 K.[60] However, perovskite devices showed thermal breakdown at lower temperature.[61] X-ray diffraction (XRD) studies on thermal degradation showed that PbI_2 formed at annealing temperatures below 373 K on prolonged annealing.[62,63] ZnO is commonly used as the ETL. Research has shown that at temperatures above 356 K the ZnO reacts with the perovskite

degrading it to PbI_2, greatly reducing the overall efficiency of devices if they are heated above that temperature.

PbI_2 that is formed during degradation is a detriment to device performance, as PbI_2 has lower charge transport properties than the perovskite. During degradation a large excess of PbI_2 causes a drop in performance due to the loss of charge transport and a simultaneous loss of charge generation (since PbI_2 does not have a favorable band gap for photocurrent generation). This means that as the devices degrade, the photocurrent is lost, and the series resistance rises.

Another thermal effect is that at elevated temperature the cubic structure is preferred. The transition temperature is at 327 K, which is accessible by photonic heating at one sun intensity. This change in crystal structure is observable as there is difference in the diffraction patterns that can be detected XRD. What is unknown is how this change in crystal structure affects the formation of hydrates or the stability of hydrates that are formed.

The other major pathway of concern is the degradation of the perovskite in the presence of oxygen.[42,64] The main pathway for oxygen degradation happens only when the device is exposed to light or has a bias put across it. This is due to the formation of superoxide (O_2^-) [64] which reacts with the methylamine in the perovskite structure.

1.3.3. Electrode Stability and Structural Integrity

Another type of degradation occurs by a reaction with the device electrode. If I^- ions are transported across the interlayer[65–67] to the metal electrode of the device, corrosion can occur if the electrode is not stable to the I^-. If the electrode is made of silver, then the silver will react and form silver iodide at the metal/interlayer interface. Due to the insulating nature of silver iodide a tiny amount of I^- transport can cause a significant decrease in device performance. This effect can be minimized though the use of corrosion-resistant electrode materials, such as gold.

When impurities such as PbI_2 are left in the film from initial processing, the perovskite film integrity is high as it forms around the PbI_2 impurities. However, as PbI_2 forms in the active layer as a result of degradation, the unit cell volume is not the same as the perovskite material. This is results in gaps forming in the perovskite as the volume of the film shrinks. This change in volume also has mechanical effects on the device layers.

In perovskite films the crystalline degradation products have different unit cell parameters that result in expansion/reduction of cell volume depending on what is being formed. The hydrates have a larger cell volume than the base perovskite material, causing strain in the film and on interlayers in the devices. This strain can cause mechanical stress in the layers as the cell volume increases. Further degradation into PbI_2, which has a lower cell volume than the base perovskite, leads to gaps between the grains and between the active layer and the interlayers. This expansion and contraction of the active layer can cause cracks in the device or total mechanical failure. The formation of these cracks means that humidity has a direct vector into the perovskite material, further increasing the degradation of the perovskite material.[68] The formation of holes allows for a direct connection between the two electrodes and decreases the shunt resistance of the device.

The expansion and contraction of the active layer has another effect on devices. The mechanical stress can result in the delamination of layers resulting in air gaps between the layers. This means that device performance can drop over time if there is multiple cycling between high and low relative humidity (RH) even if there is full reversion of hydrates back into the active perovskite material.

One of the ways to minimize the effect of mechanical strain on the device is to use materials the are flexible or robust enough to resist cracking. A case for improving resistance to

cracking involves using polymers in the interlayers. P3HT has been shown to have improved resistance to cracking over the common small molecule spiro-OMeTAD.[68] Another advantage of using P3HT over spiro-OMeTAD is that it uses less lithium dopant to increase its conductivity. By having a lower amount of ions present in the ability of water to cross the layer is reduced. This means at high RH the P3HT will have a higher stability over an equivalent spiro-OMeTAD device. This unfortunately also results in reduced device efficiencies so current best practices use spiro-OMeTAD to get the best efficiency with the focus on changing the perovskite material to be more stable.

We know that these degradation pathways are present in perovskite devices, but what is not known is the exact correlation between degradation and cell performance. Most studies have only done analysis after the devices are degraded, or else the sampling interval is sparse. Experiments that test degradation using *ex situ* methods are also problematic there are changes in the environmental conditions during the measurement process.

1.4 Grazing Incidence Wide Angle X-Ray Scattering (GIWAXS)

1.4.1. X-Ray Diffraction

To analyze the crystal structure of perovskites and their degradation products, XRD is a powerful tool. Different diffraction techniques have been used on perovskites, from single crystal XRD to solve the structure of both perovskites and their degradation products,[38,42,43,52,68–71] to powder XRD (pXRD) to analyse thin films of perovskites and devices.

The process of acquiring an XRD pattern requires that the material is crystalline and not amorphous due to the nature of how X-rays interact with a material. When an incoming X-ray interacts with the electron cloud of an atom it scatters off the atom. When it scatters off of

multiple atoms it causes the scattered electromagnetic waves to interact with one another in either a constructive or destructive manner. If the atoms have long range order like in a crystal, then we will see clear regions of destructive and constructive interference will be observed.

These areas of constructive and destructive interference follow a specific mathematical relationship known as Bragg's law (Equation 3). Lambda (λ) is the wavelength of the incoming X-ray, d is the spacing between the lattice planes in the crystal, and theta (θ) is the angle of the incoming X-ray with respect to the lattice plane. If the incoming X-ray is monochromatic then the scattering angle for constructive interference is based on the distance between two diffracting planes. Since different crystalline structures have different lattice spacing, the angle of scatter can be used as a source of structural information. This makes XRD an excellent tool to differentiate between different crystal structures.

Equation 3: Bragg's Laws

$$n\lambda = 2d \sin\theta$$

With a solved single crystal structure as a reference, we can use pXRD to determine the identity of a crystalline material in powders and thin films. The resulting data (e.g., Figure 1.13) has peaks corresponding to all of the crystalline materials present in the sample. This tool can then be used to take snapshots of the bulk crystal structure in the material at different times, revealing how the structure changes over time. For perovskites, pXRD has been used as a way to measure the quality of films, monitor changes in crystal structure as films undergo degradation, and measure the crystalline impurities present in films.

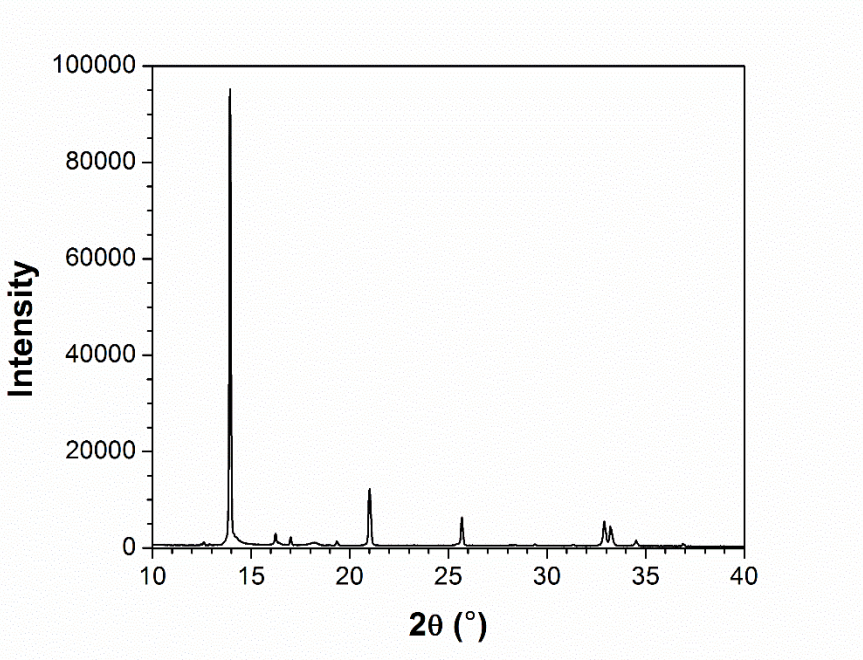

Figure 1.13 Diffraction pattern of $MAPbI_3$ with a Cu $K_{\alpha 1}$ source.

One of the properties that makes XRD so useful is that depending on the energy of the X-ray used, it can fully penetrance through all layers of the device, and the crystal structure of all crystalline layers can be monitored. This means that the perovskite layer in full devices can be monitored quite easily. Usually in pXRD the resulting diffraction patterns are a bulk measurement. If measurements are made below the critical angle of reflection, only the first ~5 nm of the film is probed due to the evanescent wave effect; if measurements are made above the critical angle, bulk measurements can be made using the same machine.

One of the key parameters in a XRD diffractometer is the X-ray source, which is generated by an X-ray tube with the energy dependent on the metal used in the tube. The energy of the X-rays is generally due to the K-alpha emission lines of the metal, which is the energy released by an electron in the $2p_{1/2}$ or $2p_{3/2}$ energy levels as it drops into the 1s orbital. Since the emission lines are different energies and we want to have a monochromatic beam, a monochromator is used to ensure that only one energy hits the sample. The flux generated by the

X-ray tubes on benchtop pXRD diffractometers means that 10-50 minutes is required to generate a diffraction pattern (depending on the range of 2θ scanned and the properties of the material). To improve on this there are other sources of X-rays that can be used for XRD experiments.

1.4.2. Synchrotron Light Source

Synchrotrons use high energy electrons at relativistic speeds to generate high brilliance broad spectrum light. The specifics of how the light is generated is beyond the scope of this thesis; what will be discussed, and what is important to a user, is what happens to this light at a beamline and end station.

When the generated light comes out of the synchrotron, it is a fan of polychromatic light. The intensity and energy distribution of this light is based on the synchrotron operating energy (generally in the low GeV range) and operating current (100's of mA range) of the facility. The properties of the emitted light are based on how powerful the magnet is that bends the electron beam and how many times it bends if an insertion device is used at the beamline.

For a hard X-ray beamline that is used for XRD on perovskite materials, the incoming light goes through apertures to block excess scattered X-rays, and the remainder then goes through filters and windows that remove the low energy photons (IR, visible, soft X-ray), leaving a polychromatic X-ray beam. That beam then goes though a monochromator generally made from a single crystal of Si or Ge; the energy range that the beamline can tune to is based on the material and lattice orientation of the crystal in the monochromator. The wavelength of X-rays is too short to make use of the diffraction gratings used in optical setups for visible light. The final beam size is then set with a set of vertical and horizontal beam slits. As a note there are usually multiple other apertures located through the beamline and all the optical components are in an ultra high vacuum environment.

Once the X-rays reach the end station they have traveled several meters from the original source; this means that the angular deviance is small and the photons can be considered collimated. If the X-rays need to be truly collimated, then the X-rays need to go through collimating optics prior to use, but this is experiment dependent. For the XRD experiments in this thesis no additional collimating is required. With hard X-rays the end station can be in open atmosphere as the air will not scatter the X-rays; if lower energy x-rays are used, then flight tubes and a sample chamber that are either under vacuum or filled with helium might be required to obtain a cleaner diffraction pattern. The sample specific setup at the end station is dependent on the experiment that the user is running; for this thesis, only the setup for preforming GIWAXS will be discussed.

For GIWAXS the general setup is that the incident monochromatic X-ray beam hits a sample at a grazing angle. The sample stage needs to have accurate controls for sample height and pitch (Bragg angle); x and y translation, roll, and yaw are also useful controls but not as important as the first two. When the incident X-ray beam hits the sample it causes it to scatter; if we want to measure the wide angle X-rays (as they measure structure on the order of 0.1-3 nm), it requires the detector to be closer to the sample. Due to the wide angle of the scatter, care needs to be taken to ensure the scattered X-rays are not blocked by anything. The scattered X-rays are then collected on a 2D detector to be analyzed; the specifics of analyzing the diffraction patterns will be discussed in section 2.4.2. The size of the sample analysed is based on the size of the incident beam, but due to the grazing angle (0.3-3°) used, the beam footprint will be large in one direction. This can cause some broadening in the diffraction pattern and a large amount of glass scattering, but adjustments to sample height before starting the experiment can result in a cleaner diffraction pattern. The output data for a GIWAXS experiment is a 2D scattering pattern, an

example of which is shown in Figure 1.14. The pattern for a powder with non-preferentially (random) oriented crystal faces has a ring like structure. If there is preferential orientation of the crystal faces (like in Figure 1.15) then the scattering pattern is no longer concentric rings but starts to have a speckled look and the intensity varies along the ring path. Based on where the intensity is brightest, the preferred orientation of the crystallites can be determined. Near the center of the scattering pattern (along the q_z axis) the lattice planes stack normal to the substrate; near the edge (along the q_{xy} axis) the lattice planes stack parallel to the substrate.

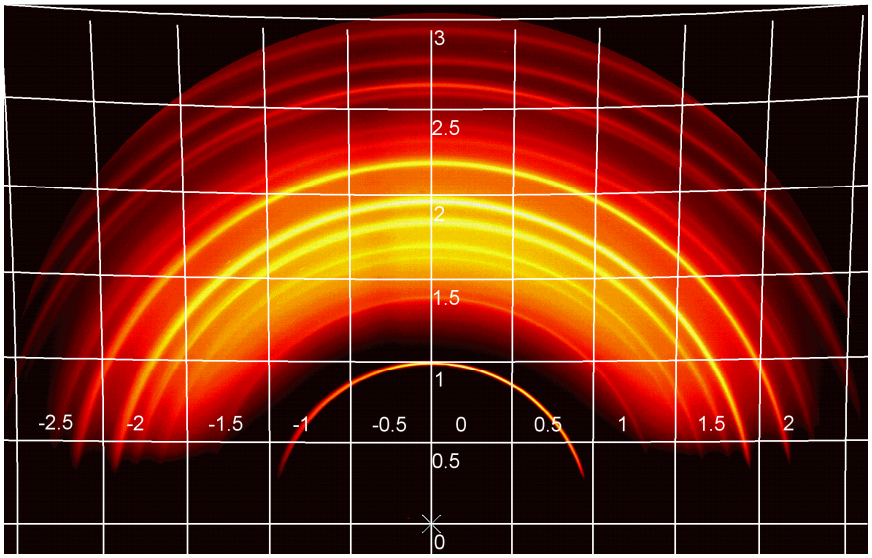

Figure 1.14 GIWAXS 2D diffraction pattern of a full perovskite device on FTO coated glass with ZnO ETL, P3HT HTL, and Au top electrode with q_z-q_{xy} grid overlay. Units are in $Å^{-1}$

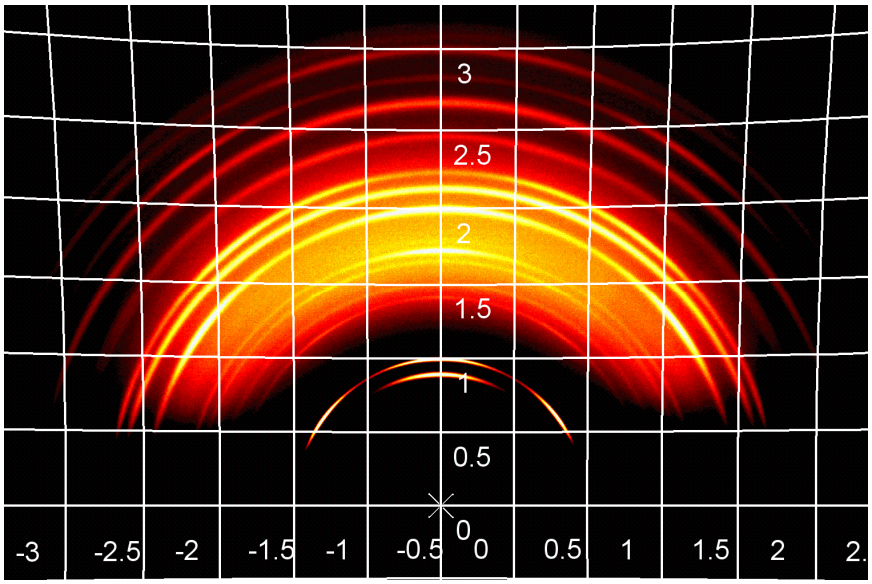

Figure 1.15 GIWAXS 2D diffraction pattern of a full perovskite device on FTO coated glass with ZnO ETL, P3HT HTL, and Au top with PbI_2 impurities and preferential orientation with q_z-q_{xy} grid overlay. Units are in $Å^{-1}$

The GIWAXS patterns require an acquisition time of 3-60 seconds depending on the experimental parameters. This means that fast and accurate patterns can be obtained with GIWAXS, making this a very useful and versatile tool to analyze thin films undergoing chemical change.

1.4.3. Application of GIWAXS to the Study of Lead Halide Perovskites

There are many groups that have applied GIWAXS to study perovskite solar cells. Yang *et al.*[53,68] used GIWAXS to measure perovskite films and devices *in situ* as they were exposed to high RH in an environmentally controlled chamber. They used GIWAXS to probe the active layer in films and devices to determine the mechanism of degradation of the perovskite layer. They were able to measure the stability of a film to determine the length of time it takes to

degrade the film under conditions of ~98% RH and 22 °C. In the same study, they used different HTLs to determine how they affected the stability of the perovskite layer. They concluded that a polymer material such as P3HT was better able to adapt to changes in film morphology and maintain coverage versus a small molecule such as Spiro-OMeTAD. In a follow up publication they used a similar setup to measure the lifetime of thin film perovskites on flat and mesoporous ETLs. Here they noticed that the perovskites on mesoporous ETLs had a substantially increased lifetime versus flat ETLs. This is due to the perovskite entering the pores of the ETL which protect the perovskite from moisture incursion.

In work done by Snaith and Wiesner *et al.*[72,73] they used GIWAXS to monitor perovskite crystallization during the processing and formation of the films. In the first publication they used a $MAPbCl_xI_{3-x}$ active layer on mesoporous Al_2O_3. They first used GIWAXS to monitor the crystallization and orientation of perovskite films with different concentrations of chloride ions. They continued to perform annealing studies on these films to determine how they form. During the study it was found that an unknown precursor phase of the perovskite was formed after casting. As the annealing temperature was increased, the precursor structure was transformed into the perovskite structure. If annealed for too long, the perovskite started to degrade and PbI_2 formation was seen in the diffraction patterns. In a second study by the same group, they compared different growth methods on mesoporous Al_2O_3. Here they used GIWAXS to monitor crystal growth of the perovskite under two different annealing conditions: 100 °C for 45 min and 100 °C for 5 min then 130 °C of min. The GIWAXS measurements showed the phase transition from the precursors to the perovskite. Through GIWAXS they were able to determine that complete conversion to perovskite happened for all samples; they were also able to determine

that different mesoporous Al_2O_3 scaffolds help the perovskite crystallites to preferentially orient on the substrate surface.

Grätzel *et al.*[74] used GIWAXS to probe a new HTL (CuSCN) that they used with a mixed perovskite ($CsFAMAPbI_{3-x}Br_x$) active layer. Here they were able to determine that the β-CuSCN polymorph formed instead of the α-CuSCN polymorph. The β-CuSCN, which forms in large sheets, also grew with a preferential orientation that was normal to the perovskite active layer. The devices made using this HTL had an average device efficiency of 19.2 ± 0.8% and when encapsulated in poly(methyl methacrylate) retained 95% efficiency under one sun intensity and 60 °C temperature for 1000 hours.

GIWAXS has a wide range of applications in perovskite solar cells, and is also applicable to other crystalline materials. GIWAXS methods can be used to determine structure, orientation and film quality of the perovskite layer and the layers around it. The new protocols and experimental setups involving GIWAXS that are developed as part of this thesis may therefore also be applicable to other materials and devices.

1.5 Objectives

The objective of this work is to develop an experimental setup and protocol to perform GIWAXS on a fully functional perovskite solar cell, during operation. This setup will then be used inside an environmentally controlled chamber to perform *operando* degradation of a perovskite solar cell. The time correlated data from these measurements will then be used to gain insight into how structural changes affect the PCE of devices. Correlated data with sufficient time resolution will allow a deeper understanding of what is happening to the solar cell as the perovskite is in the process of degradation. Two different device architectures will be compared: one with a silver back contact, and one with a gold back contact. The results will be discussed in

chapter 3, and a summary of the work and future uses of the experimental setup will be discussed in chapter 4.

Chapter 2 Experimental

2.1 Material Synthesis

2.1.1. Materials

Poly(3-hexylthiophene) (P3HT, electronic grade) was purchased from Rieke Metals. Lithium bis(trifluoromethane-sulfonyl)imide (Li-TFSI, 99%), lead(II) iodide (PbI_2, 99%), 4-*tert*-butylpyridine (96%), methylamine (33 wt.% in absolute ethanol), hydriodic acid (57% in H_2O), and titanium diisopropoxide bis(acetylacetonate) (75 wt.% in isopropanol) were purchased from Sigma Aldrich. Ag pellets (99.99%) and Au pellets (99.99%) were purchased from Kurt J. Lesker. ITO coated glass (25 mm x 25 mm x 1.1 mm, R_s = 15-25 Ω/□) was purchased from Delta Technologies. FTO coated glass (300 mm x 300 mm x 3.3 mm, R_s = 7 Ω/□) was purchased from Sigma Aldrich and cut down to size (25 mm x 25 mm x 3.3 mm). All other chemicals were purchased from Fisher Scientific and used as received.

2.1.2. Methylammonium Iodide

Hydriodic acid (20 mL, 57% in H_2O, 0.15 mol) was added to a 250 mL round bottom flask containing a stir bar and cooled in an ice bath. While stirring, methylamine (20 mL, 33% in absolute ethanol, 0.16 mol) was added to the hydriodic acid. The solution was stirred for 2 hours, then the solvents were removed by evaporation under reduced pressure at 60-75 °C. The brown crude product was successively recrystalized from hot ethanol by the addition of diethyl ether until white crystals were formed. The crystals were dried under high vacuum at 60 °C for 6 hours.

2.1.3. ZnO Nanoparticles

In a 500 mL round bottom flask zinc acetate dihydrate (2.95 g, 0.013 mol) was dissolved in 100 mL of methanol. In a dropping funnel potassium hydroxide (1.59 g, 0.028 mol) was dissolved in 80 mL of methanol. The potassium hydroxide solution was added dropwise over 10 minutes to the zinc acetate solution while it was stirring at 800 rpm at 70 °C. After addition the solution was stirred at 1200 rpm at 80 °C for 1 hour. The solution was then stirred at 1000 rpm at 70 °C for 1.5 hour. The nanoparticle solution was removed from the heat and allowed to settle for 2.5 hours. The supernatant was decanted, and the nanoparticles in the residue were concentrated by centrifugation (5000 rpm for 5 min).The supernatant was decanted, and the residue was then dispersed into ~40 mL methanol by sonication. This was then concentrated, the supernatant decanted, and the residue dispersed two more times to complete the washing procedure. The nanoparticles were dispersed in a mixture of 40 mL of 1-butanol and 3.5 mL of chloroform. The solution was analyzed by dynamic light scattering to ensure nanoparticle size was ~ 6 nm, and the ZnO concentration was measured by evaporating the solvent from a small sample and weighing the dry nanoparticles. ZnO nanoparticle solution was then diluted down to a concentration of 6 mg/mL prior to spin coating.

2.1.4. Perovskite cell fabrication

ITO/FTO glass substrates were cleaned by sequential sonication in detergent (2% extran), acetone, and isopropanol and were UV/ozone cleaned immediately prior to use. A ~20 nm thick layer of ZnO nanoparticles was deposited by spin coating from a nanoparticle solution (6 mg/mL in butanol). The ZnO nanoparticle solution was static cast onto a cleaned ITO/FTO substrate then spun at 500 rpm for 3 seconds then 3000 rpm for 25 seconds, and this step was repeated two

more times per substrate. The ZnO coated ITO/FTO substrates were transferred into a nitrogen filled glovebox for storage until use.

A layer of PbI_2 (130 nm) was then deposited onto the ETL by thermal evaporation at a base pressure of $1x10^{-6}$ mbar. The films were then transferred to a humidity controlled glove bag (40% RH). While in the glove bag the films were dipped into a solution of CH_3NH_3I in isopropanol (10 mg/mL) for 2 minutes, then spun at 3000 rpm for 20 seconds to dry. The process was repeated three times, after which the PbI_2 had been converted to a ~300 nm thick $CH_3NH_3PbI_3$ layer. The films were removed from the glove bag after 5 minutes.

To deposit the HTL a P3HT solution (20 mg P3HT, 3.4 μL of 4-*tert*-butylpyridine, and 6.8 μL of Li-TFSI solution (28 mg Li-TFSI/1 mL acetonitrile), all dissolved in chlorobenzene) was spin coated onto the $CH_3NH_3PbI_3$ films at 1000 rpm for 25 seconds, resulting in a ~85 nm thick P3HT layer. The partial device was then transferred to a nitrogen filled glovebox.

The top electrode for the devices was either a Ag or Au electrode (50 nm thick), and was deposited by thermal evaporation at a base pressure of $1x10^{-6}$ mbar.

2.2 Device Performance Characterization

Device performance was measured inside a nitrogen filled glovebox. The devices were illuminated with a 450 W Class AAA solar simulator (Sol3A, Newport) with an AM 1.5G filter. The illumination was calibrated to 1 sun intensity with a silicon reference cell (91150V, Newport) prior to each use. The cell area was defined as 0.101 cm^2 using a non-reflective aperture mask. The electrical data was obtained with a source-measure unit (Keithley 2400). Prior to acquisition the shutter on the lamp was opened and the devices were light soaked for 5 seconds. The acquisition parameters were a forward sweep voltage of 1.200 V to −0.100 V, 100 data points, and a 50 ms dwell on each point.

2.3 GIWAXS

2.3.1. **Objective**

The first goal of the thesis was to develop a test platform that allowed the acquisition of GIWAXS data at a synchrotron beamline while allowing I-V measurements to be acquired simultaneously. This means the sample holder must allow for light from a lamp to reach the transparent side of the device. The X-ray beams need to hit the thin film side of the substrate, and the resulting scatter needs to reach a 2D X-ray detector unobstructed by any equipment, electrodes, and support structure.

The whole *operando* sample holder then needs to be encased in a chamber that can be environmentally controlled. This sealed chamber needs to preform the desired function without interfering with the operation of the *operando* sample holder. The chamber also needs access points to allow for easy change out of samples.

The chamber then needs to be mounted to a stage and configured in a way to allow for the sample to be easily aligned to the beam with minimal disturbance from changing samples. Once these functions have been achieved, the time corelated data can be acquired from a fully operating device while it is degrading, and the data analyzed.

2.3.2. Chamber Design

The experiments required that the chamber be able to cycle through multiple different environments and remain sealed even with peripheral equipment attached. For this, off-the-shelf components were used and modified for the experiment. The main chamber used was a (MCF450-SphCube-E6A8, Kimball Physics) spherical cube design shown in Figure 2.1. This type of chamber allows for flanges to be fitted to each port on the chamber that can be machined

to fit multiple desired components. These flanges can also be switched out for other components or blanks depending on the experiment being run. These flanges have a sealing surface onto the chamber allowing for all configurations to have a sealed environment on the inside.

Figure 2.1 Computer drawing of the Kimball Physics spherical cube (MCF450-SphCube-E6A8).[75]

For this setup that we need to worry about the requirement for X-rays to travel relatively unhindered through the chamber. For this two X-ray windows made from kapton were installed on either side of the chamber on two large 4.5” ports. Kapton is a polyimide material that has excellent characteristics, such as resistance to X-ray degradation, good transparency at the energy used in these experiments, and solvent and moisture resistance. Perpendicular to the beam, two other components were added to the chamber. One was a door that allows for access to the inside of the chamber, so that samples can be quickly changed between experiments. The other component was a glass window to allow light to illuminate the sample for the device performance tests.

The RH inside the chamber needs to be controlled. This was accomplished by using a bubbler setup based on a previous design.[68] The basic design is shown in Figure 2.2. The main idea is that a gas stream, in this case nitrogen, is split into two streams which are controlled by two mass flow controllers (MFC). One of the gas feeds goes into a set of water bubblers to be saturated with water vapour. The dry gas flow is then mixed with the saturated water vapour. The flow rates for each stream are controlled by the mass flow controllers. Changing the relative flow rates allows the RH inside the chamber to be controlled. The MFC's used (MC-5SLPM-D, ALICAT Scientific) allow for up to 5 SLPM flow rates through each line. This allows for quick flushing of the gas in the chamber to get the chamber to the desired RH quickly. These controllers can be also remotely operated which allows the chamber environment to be changed from outside the hutch.

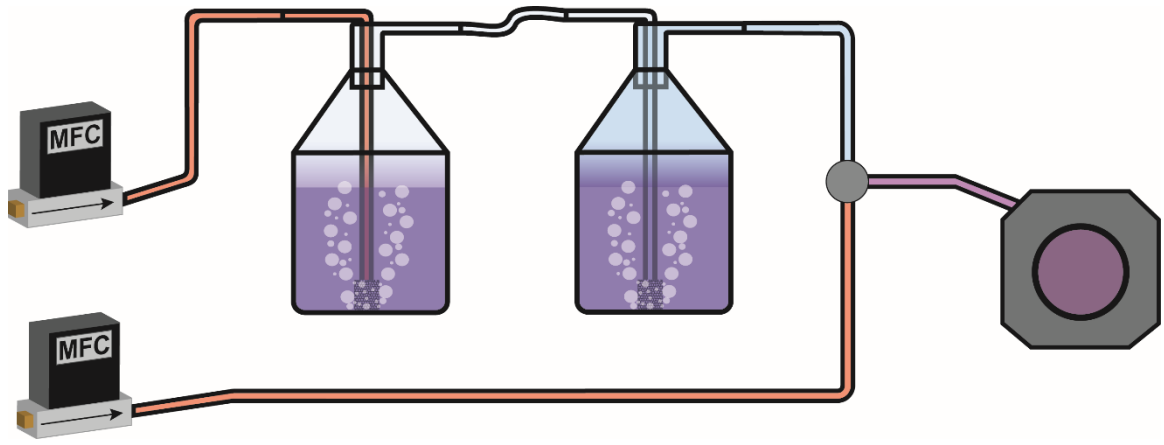

Figure 2.2 Schematic of water bubbler setup used to control the chamber humidity.

The chamber was equipped with two gas ports on either side of the chamber on the 1.33” ports. One port allowed gas to flow into the chamber from the bottom, and one port allowed gas to exit the chamber from the top. This configuration of gas flow was chosen to prevent the incoming gas from directly blowing onto the sample. This was done because the incoming gas flow may not represent the rest of the measured environment in the chamber. To make sure that the environment in the chamber is at the desired humidity a probe to monitor the RH was installed into the top flange. The humidity sensor (Omega, RH-USB) allows for remote monitoring of the chamber environment, so that adjustments can be made if necessary to maintain the desired RH.

The final peripherals are a mount on the bottom that allows the chamber to be connected to the stage assembly at the beamline to perform beam alignment to the sample. An electrical feed-through is also required for the device in the chamber to be connected to an external source-measure unit that can measure the electrical characteristics of the device. This is accomplished by a two-wire feed-through that is electrically isolated from the chamber itself. The complete setup is shown in Figure 2.3.

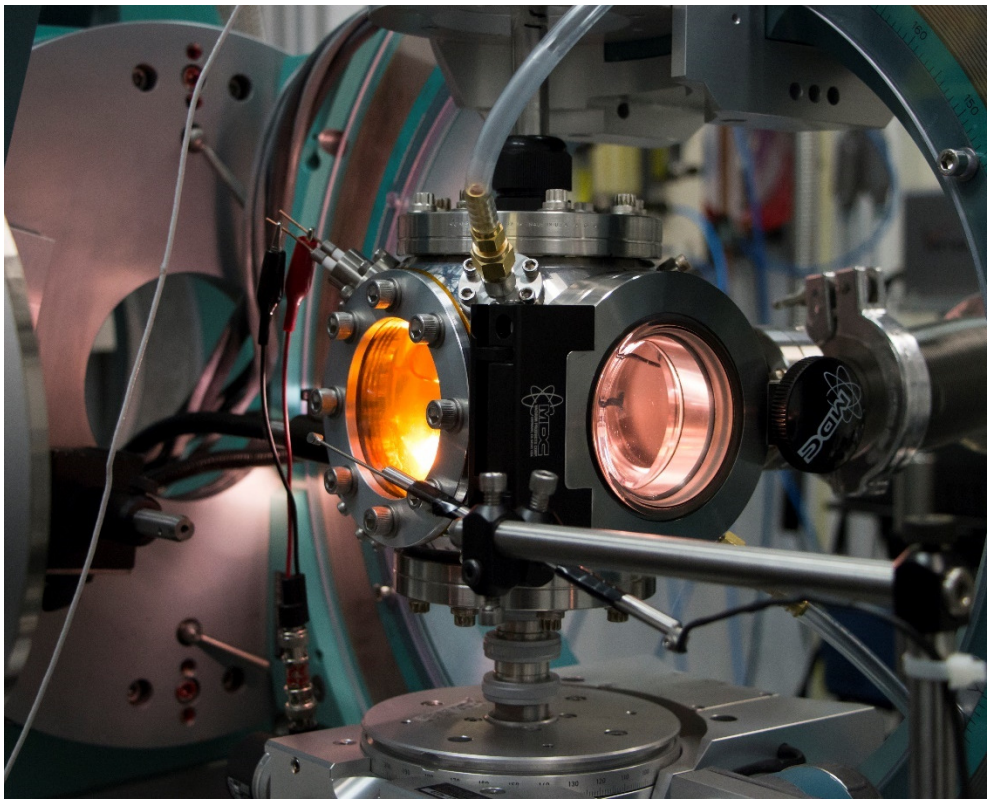

Figure 2.3 Photograph of the experimental chamber with peripheral components.

The next part of the chamber is the sample holder inside the chamber. The drawings in Figure 2.4 show how the sample holder was designed. As seen in the top view (Figure 2.4a) the sample holder has an opening in the bottom to allow light through that has been redirected from a mirror (Figure 2.4b) which illuminated the device. The sample holder also has integrated electrical connections; one of the connections is attached to a movable arm to allow it to be positioned onto the top electrode (metal) of the desired cell. The second electrode is a copper clip that clamps down on the sample and connects with the bottom electrode (ITO or FTO). This clip also holds the sample in position during the beam alignment phase.

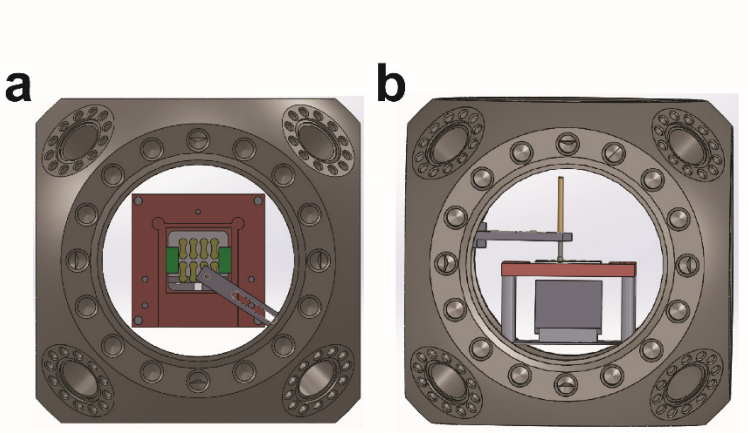

Figure 2.4 Computer drawings of the sample holder top (a) and side (b).

The sample holder also incorporates a mirror (Thor Labs, BBAQ1-E02) at a 45° angle below the opening in the sample holder. This mirror is used to reflect incoming light from the illumination lamp onto the device for bottom-up illumination. This mirror can be repositioned to ensure that the light hits the device under test. The overall setup inside the chamber is shown in Figure 2.5

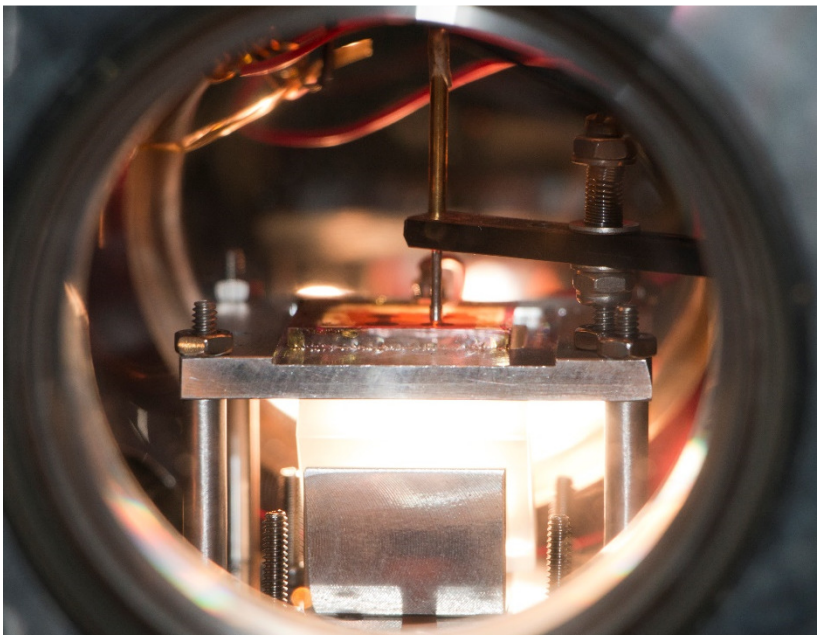

Figure 2.5 Photograph of the sample holder inside the chamber.

2.3.3. Beamline Data Acquisition

The RH of the sample chamber was controlled by bubbling nitrogen through water and mixing with a dry nitrogen gas stream that was controlled by MFC's and the RH was monitored by a humidity sensor. I-V curves were measured with a Keithley 2634B source-measure unit (1.2 to −0.2 V sweep, 100 ms delay, 120 steps). The cells were illuminated to generate a photocurrent by a fiber optic illuminator (Fiber-lite, MI-150).

GIWAXS measurements were performed at the Hard X-ray MicroAnalysis (HXMA) beamline of the Canadian Light Source (CLS). An energy of 17.998 keV ($\lambda = 0.6888$ Å) was selected using a Si(111) monochromator. The diffraction patterns were collected on a SX165 charge capture device (CCD) camera (Rayonix) using an acquisition time of 3 seconds unless otherwise stated. The sample to detector distance (~270 mm) was calibrated using a LaB_6 powder standard. For *operando* measurements the devices were placed in the sample chamber, which was flushed with dry nitrogen. An initial I-V curve and diffraction pattern were acquired. The humidity was then raised to the desired RH. I-V curves were acquired at 1 minute intervals; diffraction patterns were acquired at 3 minute intervals. All data were processed using the Datasqueeze 3.0 software package and Origin Lab Pro. The light source study was conducted with an light emitting diode (LED) bicycle lamp (CygoLite, Mity Cross) and the fiber optic illuminator (Fiber-Lite Mi-150, Dolan-Jenner), and their spectral output was measured with a spectrophotometer (USB2000+, Ocean Optics).

2.3.4. Data Processing and Analysis

The original raw data from the 2D detector can be seen in Figure 2.6. This data has a uniform ring pattern showing that there is no preferred orientation. The first thing that is done with the captured data is to calibrate it against the LaB_6 standard.

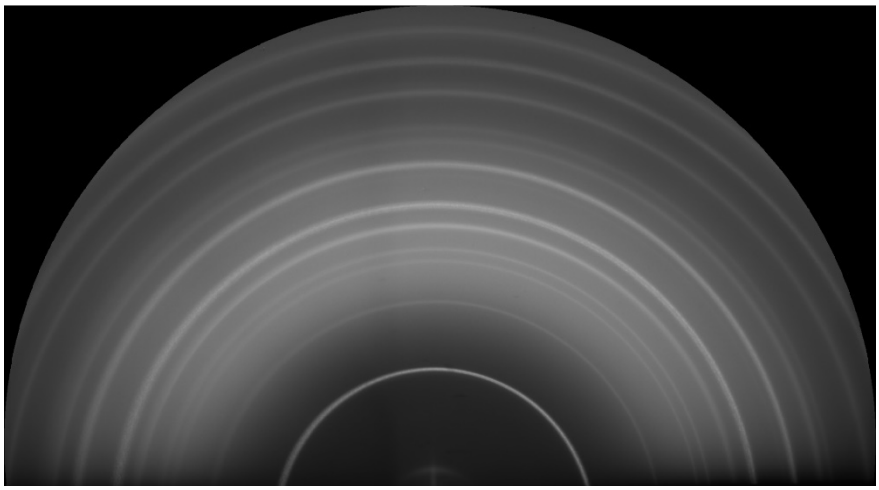

Figure 2.6 Raw detector data.

To calibrate the data in this thesis, the Datasqueeze software package was used. The data was calibrated then referenced against the (110) reflection of $MAPbI_3$ layer to ensure the sample was correctly calibrated. When the calibration is done, we obtain a 2D diffraction pattern plotted against the q_z and q_{xy} components of the scattering vector (Figure 2.7). This calibration is done for each set of data.

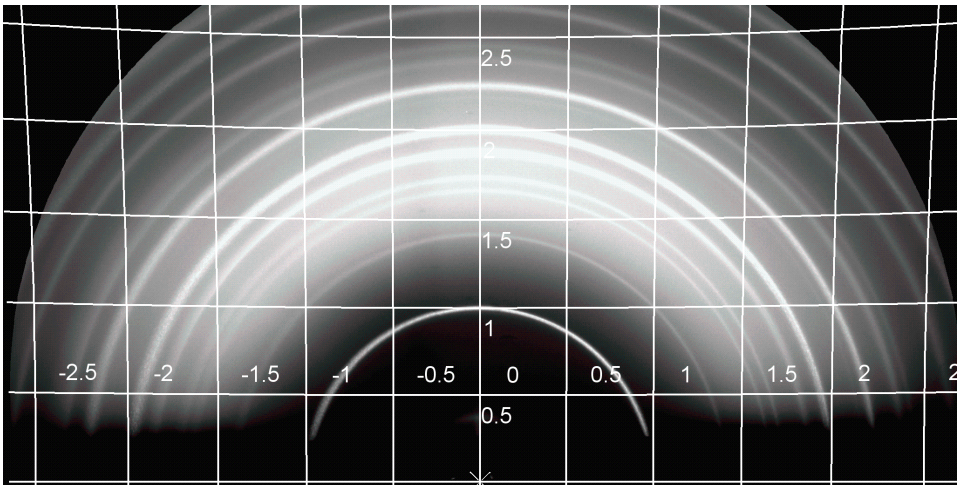

Figure 2.7 Calibrated data with q_z-q_{xy} grid overlay. Units are in $Å^{-1}$.

As there are multiple sets of data it is helpful to integrate the data azimuthally so that we reduce the dimensionality of the data (Figure 2.8a). To compensate for the changes in the ring current the data is then normalized relative to a reference peak; in this case, it is the gold top electrode, for which the (111) reflection is at 2.66 $Å^{-1}$. The resulting normalized graph is shown in Figure 2.8b.

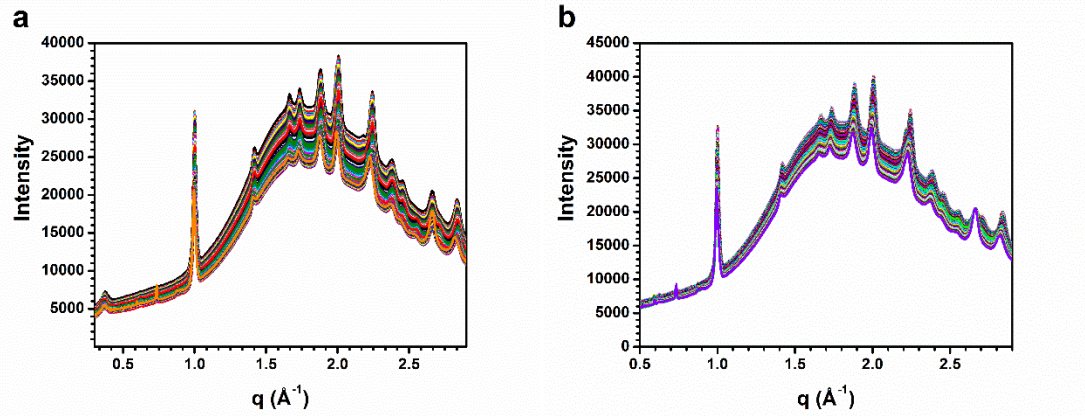

Figure 2.8 Azimuthally integrated data (a) and the same data normalized to the gold electrode (b).

To get rid of the large background that results from the scattering from the glass substrate scattering, the background is fit with a simple spline curve and subtracted from the data shown in Figure 2.9a. The resulting data set is shown in Figure 2.9b which has the glass background removed. It is important to note that the method of background subtraction is not exact. Due to the nature of the collected data it was possible to get more accurate subtractions at lower q values where there are fewer peaks and the curve can be closely fitted. At higher q values we see many more peaks and it is no longer possible to fit the curve as accurately.

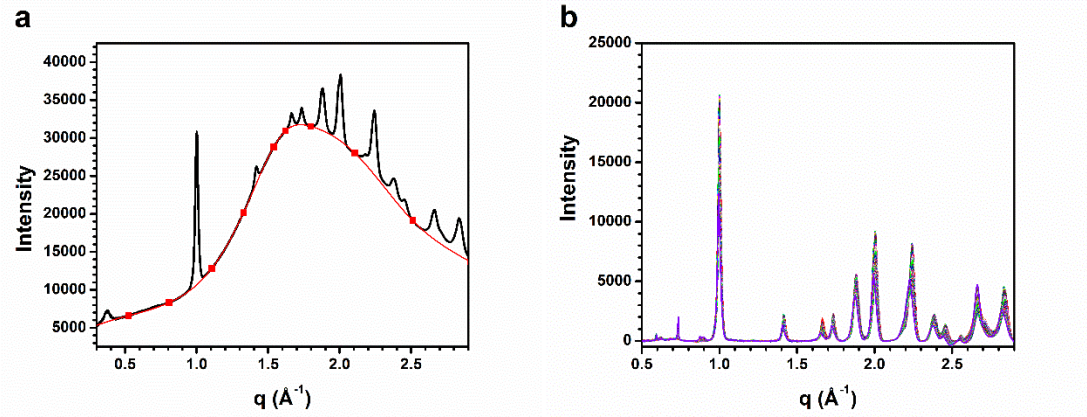

Figure 2.9 Azimuthally integrated GIWAXS data (black) showing the spline fit to the background (red) (a) and subtracted data (b).

The resulting data is then converted to a 3D graph (q, intensity, time) to show the changes in the sample as it is exposed to humidity (Figure 2.10).

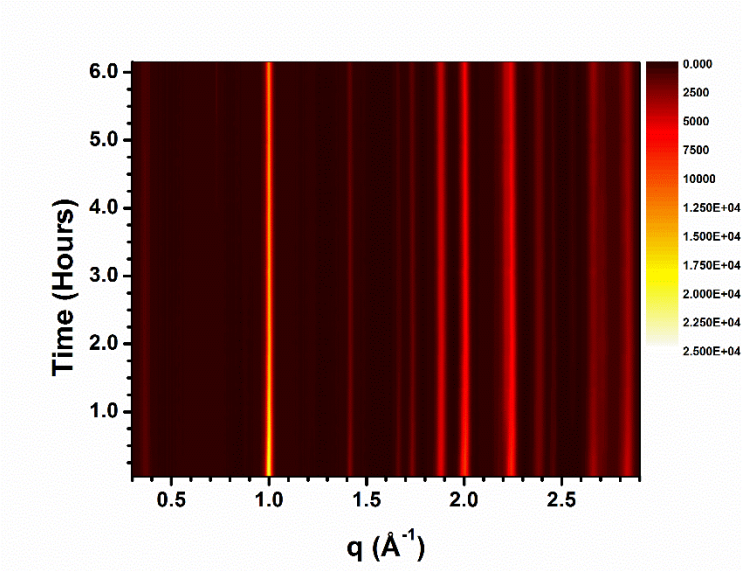

Figure 2.10 3D plot of the azimuthally integrated GIWAXS data (q, intensity) against time. The colour scale denotes the scattering intensity.

The other set of data that needs to be analyzed is the electrical data from the devices. A representative I-V curve for the initial scan of a cell is shown in Figure 2.11. The data that is extracted from the curve is the I_{sc} (y-intercept), V_{oc} (x-intercept), FF (squareness of the curve), and PCE. The characteristic values are calculated for each scan of the device, and normalized to the initial starting data as shown in Figure 2.12

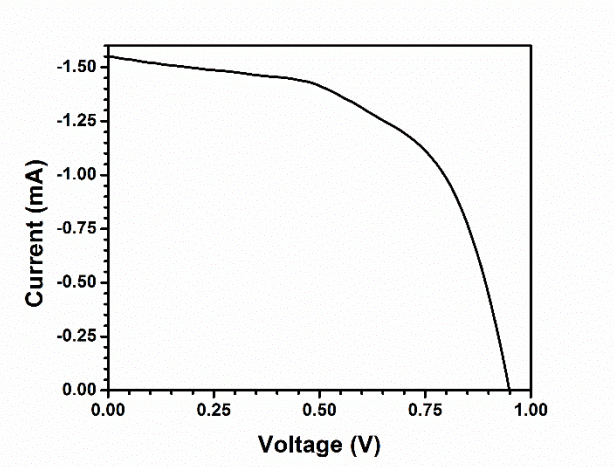

Figure 2.11 Starting I-V curve of the sample.

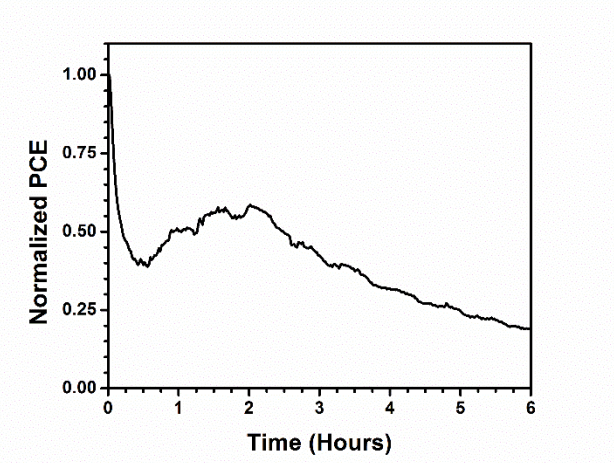

Figure 2.12 Device efficiency over time.

Since the data from both the GIWAXS and the I-V measurements are from the same device, they be can directly combined on one graph. For this the (110) perovskite peak is plotted along with the device data; the resulting plot is shown in Figure 2.13. The relationship between device performance and active layer degradation will be discussed in Chapter 3.

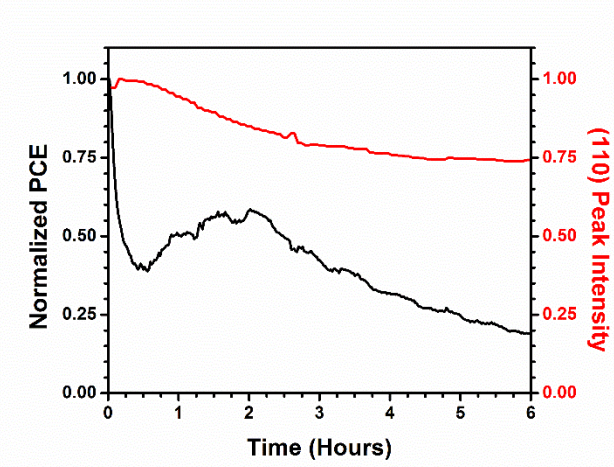

Figure 2.13 Combined GIWAXS and I-V curve data.

Chapter 3 Results and Discussion

3.1 *In Situ* experiment

The *in situ* experiments were performed on devices having either a FTO/ZnO/$MAPbI_3$/P3HT/Silver or gold architecture. The solar cells were placed in a chamber where the humidity could be changed by using a carrier gas passing through a set of water bubblers; an increase in the humidity level will cause the devices to degrade. While the devices were degraded the structural changes in the active layer were measured using GIWAXS and the device performance was measured by a source-measure unit throughout the experiment.

3.2 Silver Electrode Devices

Before devices were degraded *operando* they were characterized in a dry nitrogen filled glovebox. An example J-V curve for a device prior to degradation is shown in Figure 3.1. The devices measured in the glovebox were illuminated with a class AAA solar simulator and equipped with a shadow mask. The shadow mask defines the illumination area of the solar cell and allows currents to be converted to current densities. This enables the PCE to be calculated. By characterizing the device ahead of time, we can ensure that it has good power output and an I-V curve that does not show hysteresis.

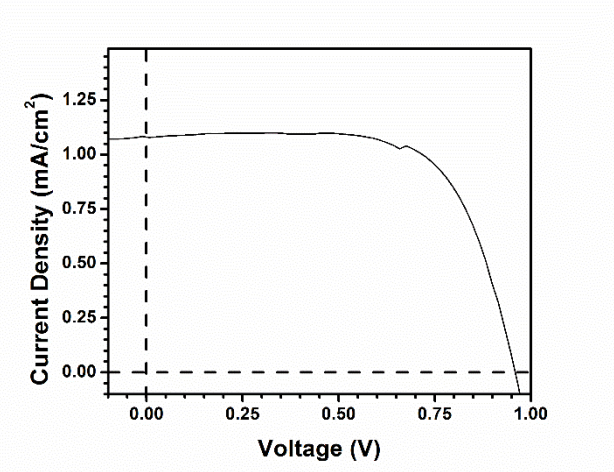

Figure 3.1 J-V curve of a solar cell in a dry nitrogen filled glovebox under a class AAA solar simulator.

3.2.1. Dry Conditions

The starting conditions for this experiment had the sample is in a dry, nitrogen purged chamber before being illuminated by the light source. The starting GIWAXS scan (shown as an azimuthally- integrated in a 1-D graph) along with the initial I-V curve for the sample are shown in Figure 3.2. From Figure 3.2a it can be seen that the device does not contain any substantial impurities, since the diffraction pattern matches the active layer ($MAPbI_3$) and the two electrodes (silver and FTO). The $MAPbI_3$ is in the tetragonal phase, as the peak at q = 1.67 $Å^{-1}$ is absent in the cubic phase. Figure 3.2b shows the device in operation. Compared to the device in Figure 3.1 this is a low quality device but for this experiment only the relative change in the performance is important. The device is first aged in a dry environment so that the behaviour of the device can be determined and compared with the results in a humid environment. Since devices can show degradation in performance due to aging and ion migration,[76] even in a dry atmosphere, it is important to separate these effects from degradation due to humidity.

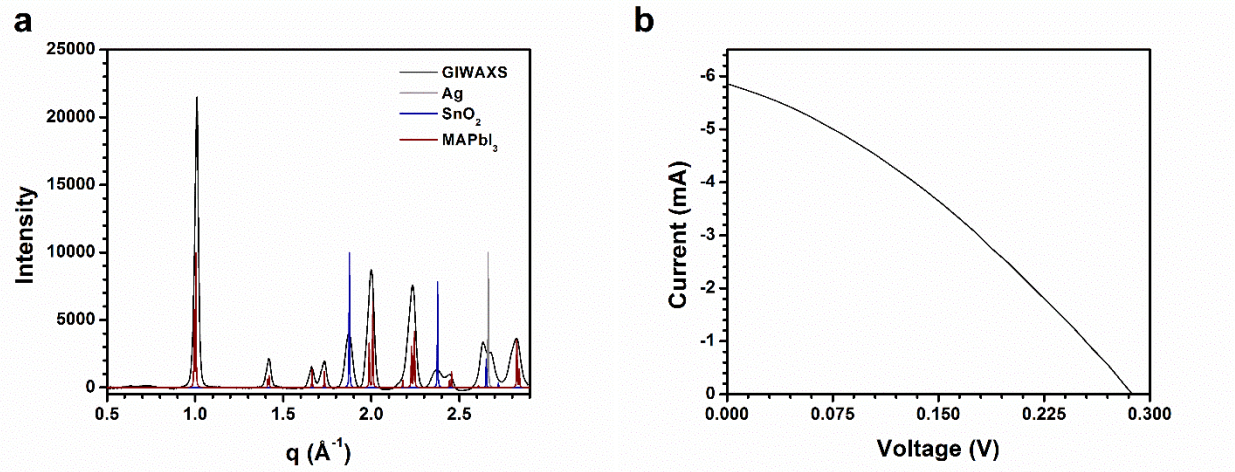

Figure 3.2 Initial GIWAXS scattering (a) and I-V curve (b) for dry silver devices.

To obtain *operando* data, the cell must be in full operation even if it does not have ideal performance. The experiment does not focus on absolute numbers, but instead on the trends in device performance with time. The experimental setup had dry N_2 constantly flowing through the chamber and the device under constant illumination. The I-V curves were measured from a 1.2 V to −0.2 V every 1 min, and GIWAXS measurements were taken every 3 min. The resulting time resolved data is shown in Figure 3.3. The GIWAXS data shows very little noticeable change in peak intensity or position over time, showing that there is little structural change in the sample. The I-V curves (Figure 3.3b) show a small drop in V_{oc} and little change in the I_{sc}.

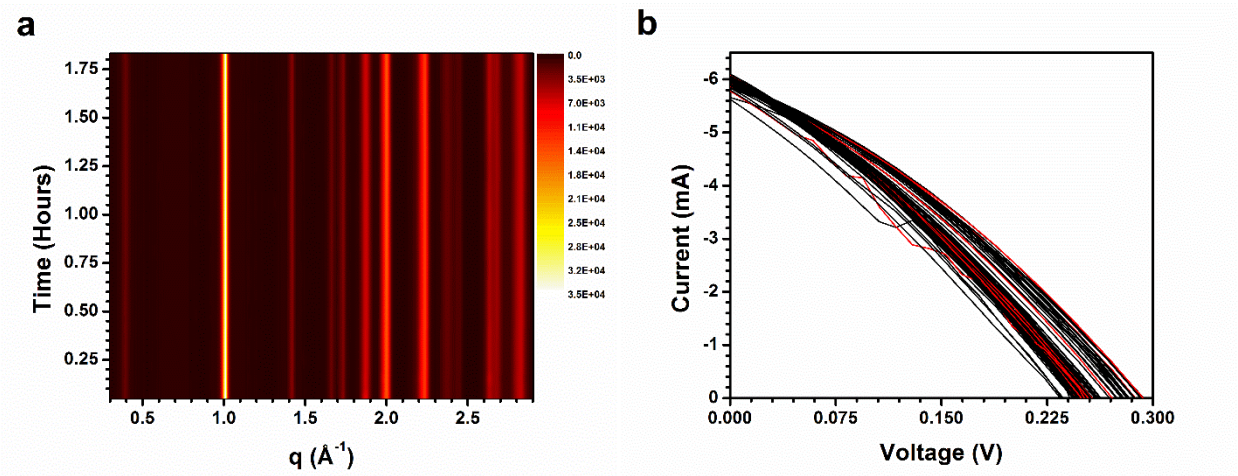

Figure 3.3 Time resolved data: (a) matrix plot of the GIWAXS data and (b) I-V curve trend for device with silver electrode at <5% RH.

When the two sets of time resolved data are compared (Figure 3.4), there is some degradation in cell performance over the course of the experiment, as seen in the I-V curves (Figure 3.3). The loss of efficiency can be attributed to a small amount of beam damage in the sample. Beam damage is radiation damage caused by the ionizing effect of X-ray beam. Another possibility is that the sample experienced some initial burn in, which is often observed in new cells. The combined effects of device burn in and beam damage likely lead to the loss in performance. However, although there is some loss of performance over time, the devices are relatively stable in the timeframe of the experiment.

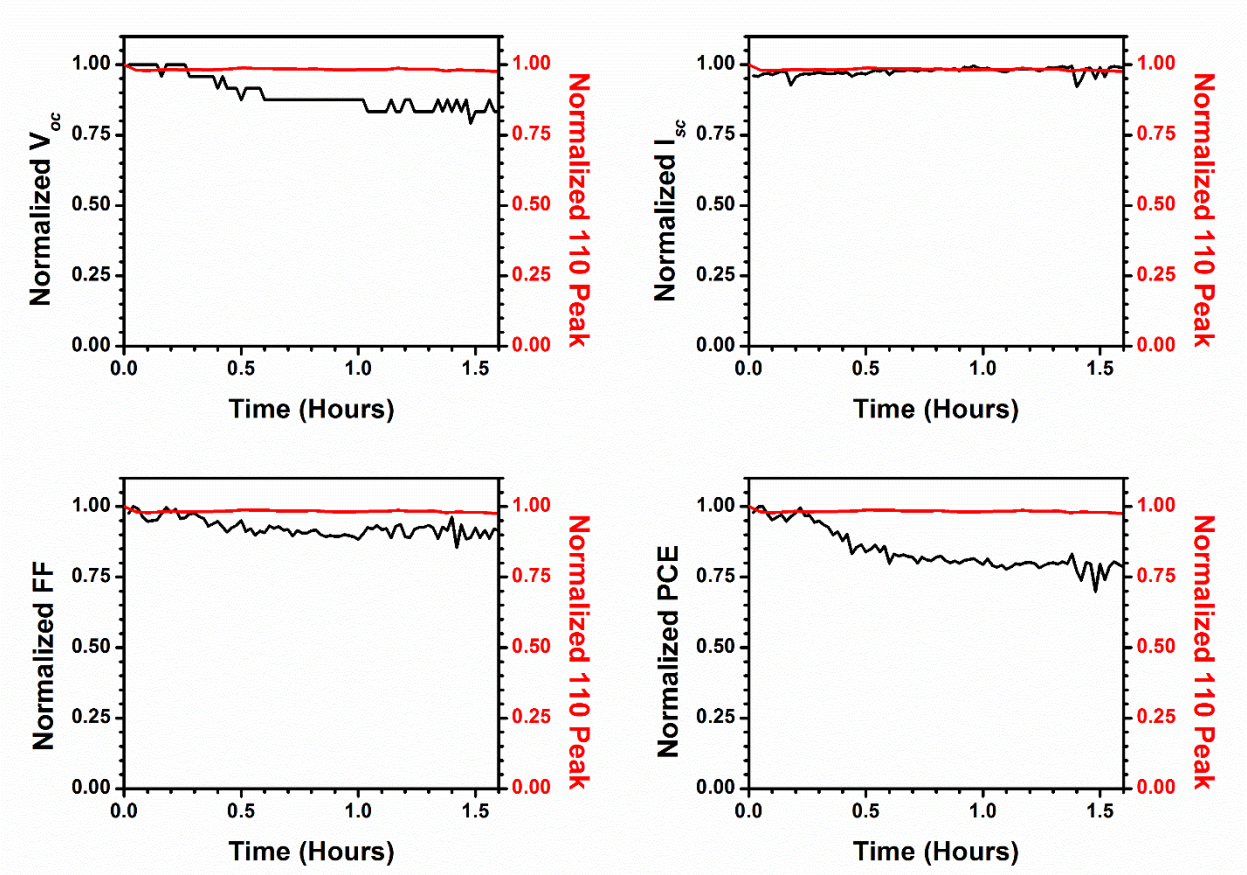

Figure 3.4 Combined GIWAXS and I-V data for device with silver electrode in <5% RH environment.

3.2.2. Wet Conditions

Having shown that there is little degradation under dry conditions, I then repeated the experiments at higher RH. The chamber was initially kept under dry conditions in order to measure the performance of a fully functional device prior to degradation. The starting GIWAXS scan (azimuthally-integrated), along with the initial I-V curve, is shown in Figure 3.5. The GIWAXS data (Figure 3.5a) shows that the device contains a small amount of PbI_2, observed from the small peak at q = 0.91 $Å^{-1}$. This impurity can happen from slight changes in the reaction conditions and is small enough to not degrade device performance. Combined with the asymmetric peaks at q = 1.67 $Å^{-1}$ and q = 1.74 $Å^{-1}$, this indicates that the sample is not phase

pure. However, the I-V curve (Figure 3.5b) shows that the device is fully functional. The higher current reading from the device is due to the halogen light source being more intense than the solar simulator used in the glovebox and no shadow mask was used.

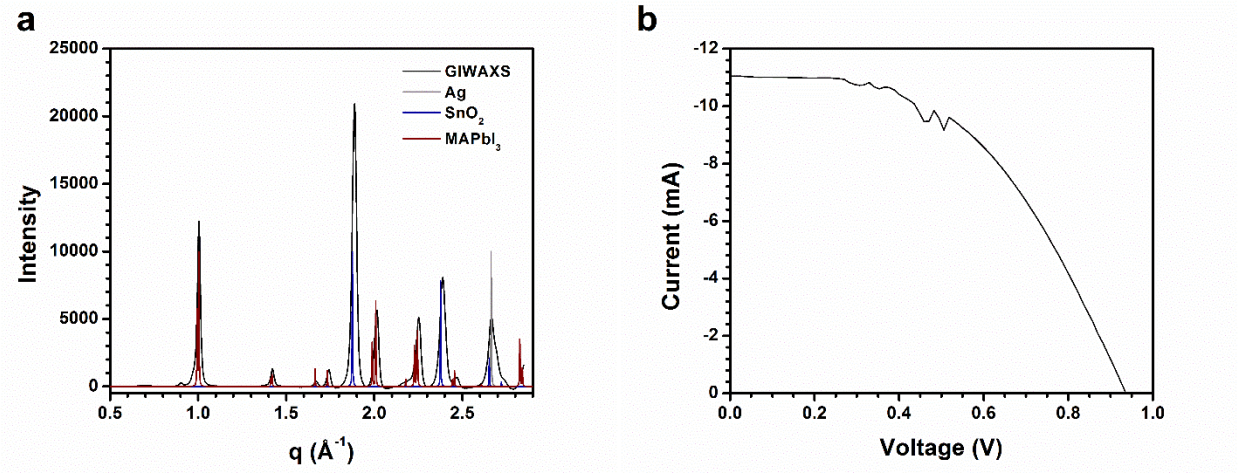

Figure 3.5 Initial GIWAXS scattering (a) and I-V curve (b) for devices with silver electrode in 80% RH.

Once the initial scans were completed, the dry nitrogen stream was replaced with another nitrogen stream that was saturated with water vapour. The humidity was monitored by a RH probe in the chamber, which recorded the RH throughout the experiment. The maximum humidity in the chamber was ~80% while the halogen light was illuminating the cell. The results from the device performance measurements were then compared to the GIWAXS data.

The time resolved GIWAXS data (Figure 3.6a) shows the trend of each reflection. As seen in the perovskite (110) peak at 1.00 Å^{-1}, the intensity does not significantly change; there is only a slight decrease in intensity over the course of the experiment.

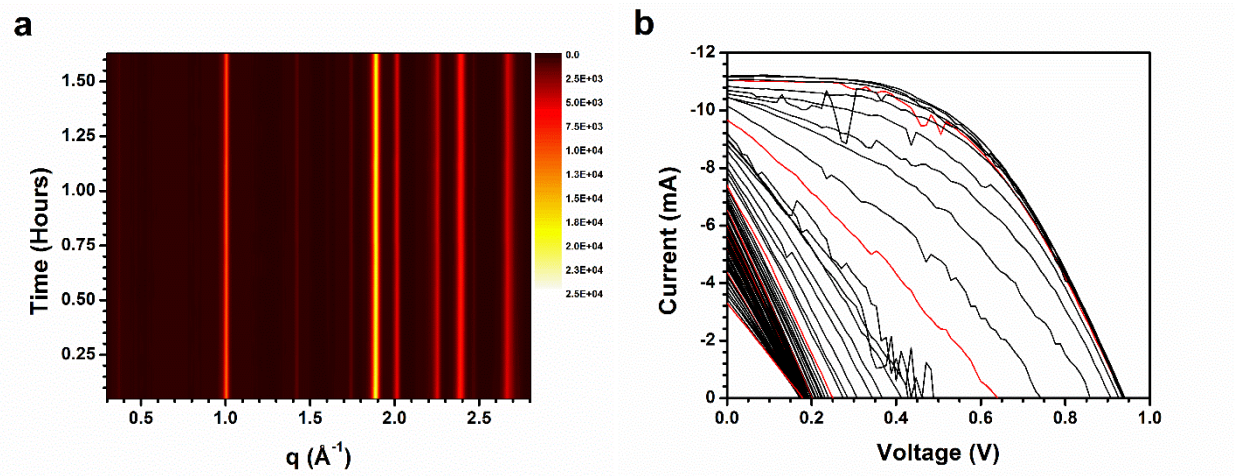

Figure 3.6 Time resolved data for: (a) GIWAXS data in a matrix plot and (b) I-V curve trend for device with silver electrode in 90% RH.

The correlated X-ray scattering and device performance data for the degradation experiment are shown in Figure 3.7. The device PCE was almost completely degraded within the first 30 minutes after exposure to higher humidity levels. From the data it can be seen that the voltage of the device decreases faster than the I_{sc}. A decrease in voltage is likely due to a change in the band gap or increase in the recombination rate in the device. Again, there was little change in either the peak intensity or position in the GIWAXS pattern, showing that the active layer was not significantly changing its bulk structure and no new crystalline by-products were being formed; there is only a slight decrease in intensity over the course of the experiment. The I_{sc} also starts to degrade. As with the device tested in dry conditions, there are still the same issues with beam damage and device burn in, which can also reduce the performance; however, the influence of these factors in the first 30 minutes was negligible.

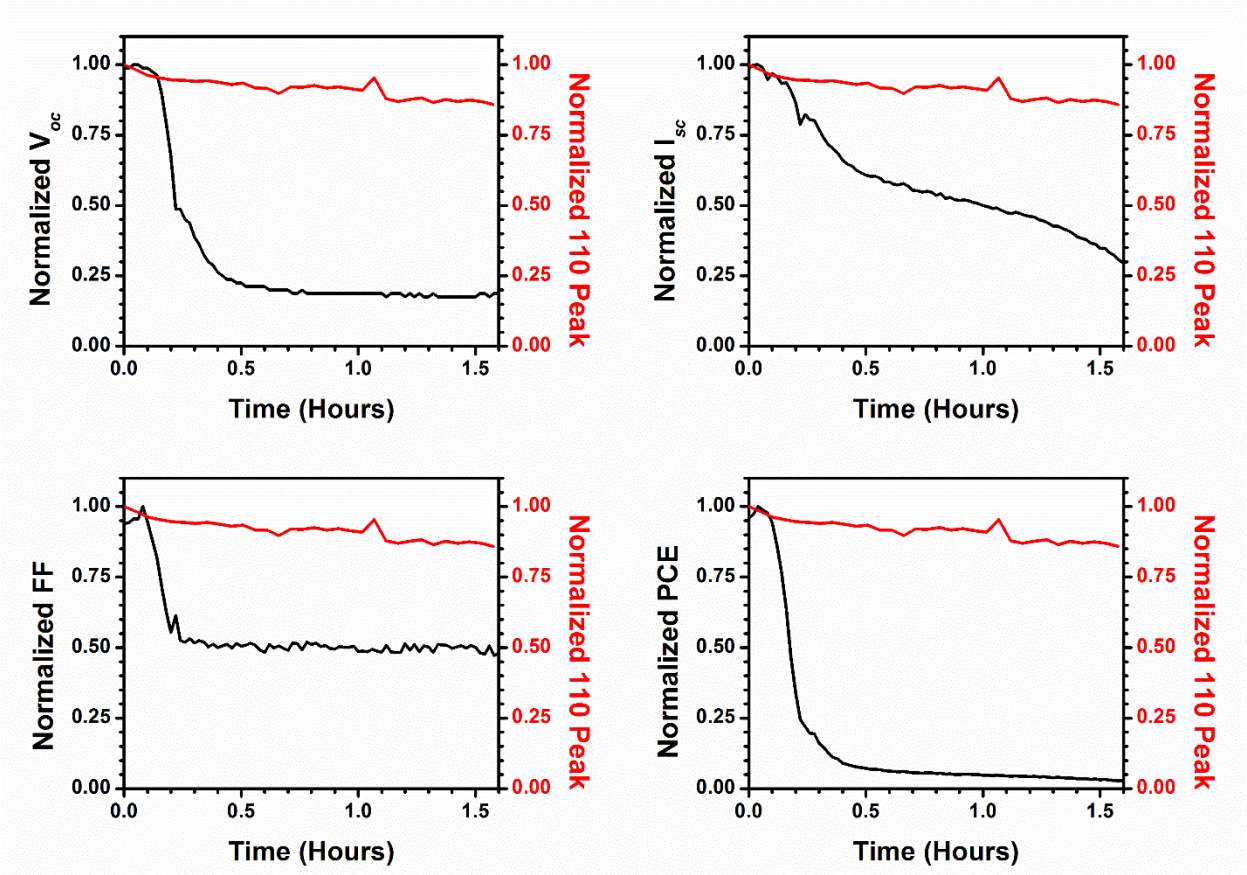

Figure 3.7 Combined GIWAXS and I-V data for silver electrode device in 80% RH.

One of the issues with perovskite devices is how moisture affects the materials in the device. One explanation for the rapid loss of PCE is an increase in the mobility of iodide ions. Iodide attack on silver electrodes has precedence in the literature,[65] where iodide can migrate through the perovskite and corrode the silver top electrode. Once iodide ions reach the silver electrode they react with the metal and form silver iodide. This silver iodide forms at the interface between the HTL and electrode. As silver iodide is not conductive like silver, the charge carriers build up at the interface between the silver iodide and the HTL, leading to an increase in the surface recombination velocity. The increase in recombination decreases the shunt resistance, which strongly affects the voltage output of the devices. This can be seen in the

V_{oc} trend in Figure 3.7. As the water penetrates the device the voltage drops much more rapidly that the I_{sc} which is indicative of an decrease in shunt resistance. The electrical data is evidence of the formation of trap states forming at the interface of the silver electrode and the HTL. Along with this build up of trap states there is an increase in ion migration in the device, causing vacancies to be present in the active layer. There will also be a corresponding increase in iodide concentration in the HTL and at the surface of the silver electrode. This results in more trap states. The net result is an increase in recombination velocity, which leads to the device losing performance quickly in the first half hour of degradation. The data obtained by the *operando* methods (Figure 3.5) shows just how quickly the iodine attack can affect the device efficiency.

An interesting observation from the GIWAXS data in Figure 3.3a and Figure 3.6a is that there was no presence of hydrates in the active layer of the device. As previous studies[68] have shown that perovskite films readily form a monohydrate phase at high RH, their absence here was surprising. Later experiments in section 3.3 will show that hydrates only form under specific conditions.

3.3 Gold Devices

Having shown that iodide can lead to oxidative corrosion of the silver the goal of this work was to determine the effect of humidity on longer lived devices with oxidation-resistant electrodes. The reactive silver electrode was replaced with a more robust gold electrode. Before devices were degraded *operando* they were characterized in a dry nitrogen filled glovebox. An example J-V curve for a device prior to degradation is shown in Figure 3.8. The same set of experiments were performed to see if there were any noticeable changes between the devices with silver and gold electrodes and if another pathway of decomposition is present in the $MAPbI_3$ devices with gold contacts.

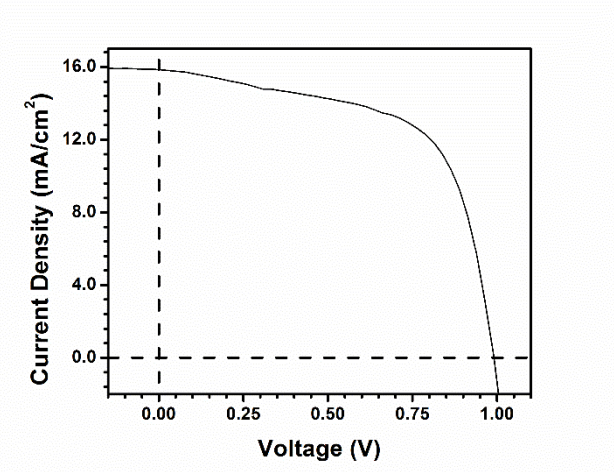

Figure 3.8 Representative a gold electrode solar cell used in the experiments that was measured in a dry nitrogen filled glovebox under a class AAA solar simulator.

3.3.1. Dry Conditions

The experiments with gold-based devices were done in the same way as the silver devices. The starting conditions for this experiment had the sample in a dry, nitrogen purged chamber before being illuminated by the light source. The starting GIWAXS scan (shown as an azimuthally-integrated 1-D graph) along with the initial I-V curve for the sample are shown in Figure 3.9. From Figure 3.9a the device contains a small amount of PbI_2 impurity, as evidenced by the peak at q = 0.91 $Å^{-1}$. The rest of the peaks correspond to the perovskite layer and device electrodes. The devices were aged in the same way as in section 3.2 to determine their behaviour. Figure 3.9b shows a lower current compared to the silver devices due to the halogen light source being lowed in intensity to better match the intensity of the solar simulator in the glovebox

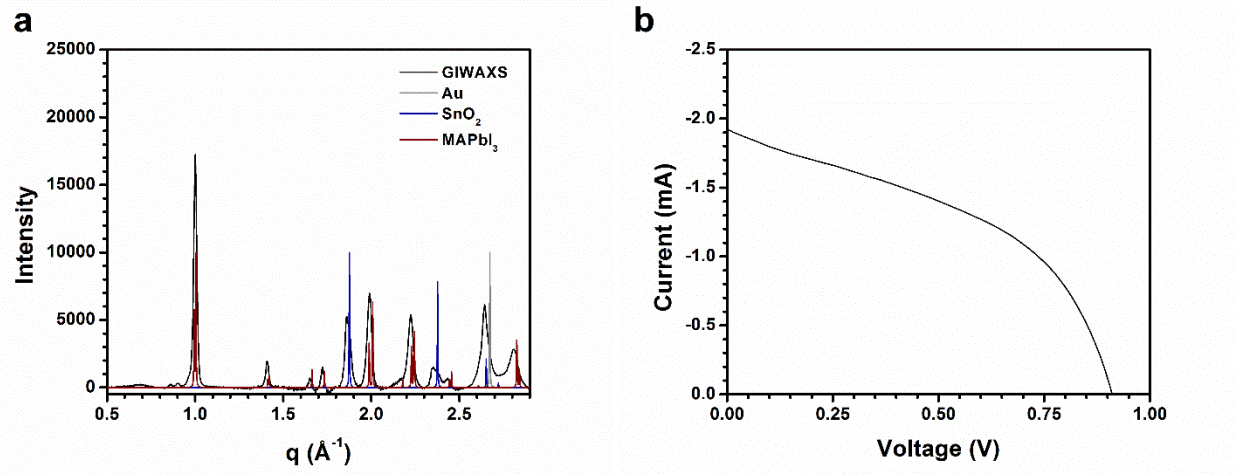

Figure 3.9 Initial GIWAXS scattering (a) and I-V curve (b) for dry gold devices.

The same degradation experiments were performed to verify that under dry conditions the silver and gold-based devices behave the same. Figure 3.10 shows the time resolved data. Similar to the silver devices the GIWAXS had no noticeable changes up to 1.5 hours; however, there were substantial changes in the I-V curves. Due to the longer life time of the device the perovskite peak was seen to decrease further into the experiment.

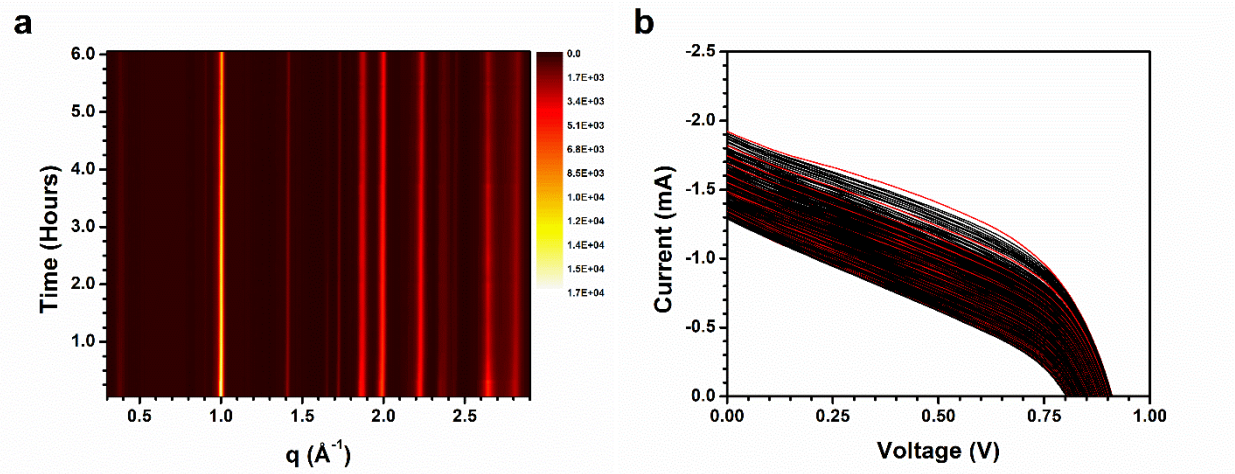

Figure 3.10 Time resolved data for: (a) GIWAXS data in a matrix plot and (b) I-V curve trend for device with gold electrode in >5% RH.

The correlated data can be seen in Figure 3.11 and we can see that there is significant degradation of the cell performance over the course of the experiment. Some of the degradation can be attributed to beam damage and device burn in. However, the major effects observed in Figure 3.11 may be due to a fabrication error. The device that was used in this experiment had a major defect in the gold electrode. The electrode was deposited in two separate steps of 5 nm and 50 nm, rather than in a single 50 nm deposition. The shadow mask moved between depositions creating a 5 nm thick gold shadow around the bulk of the electrode. A 5 nm layer of gold can consist of separate islands of gold that do not interconnect. When the device undergoes the initial burn in phase, it is possible that these thinner regions break down, leading to the observed drop in device performance. The larger area electrode may also cause problems, as there is a higher chance of encountering pinholes or other defects that can be present in the films.

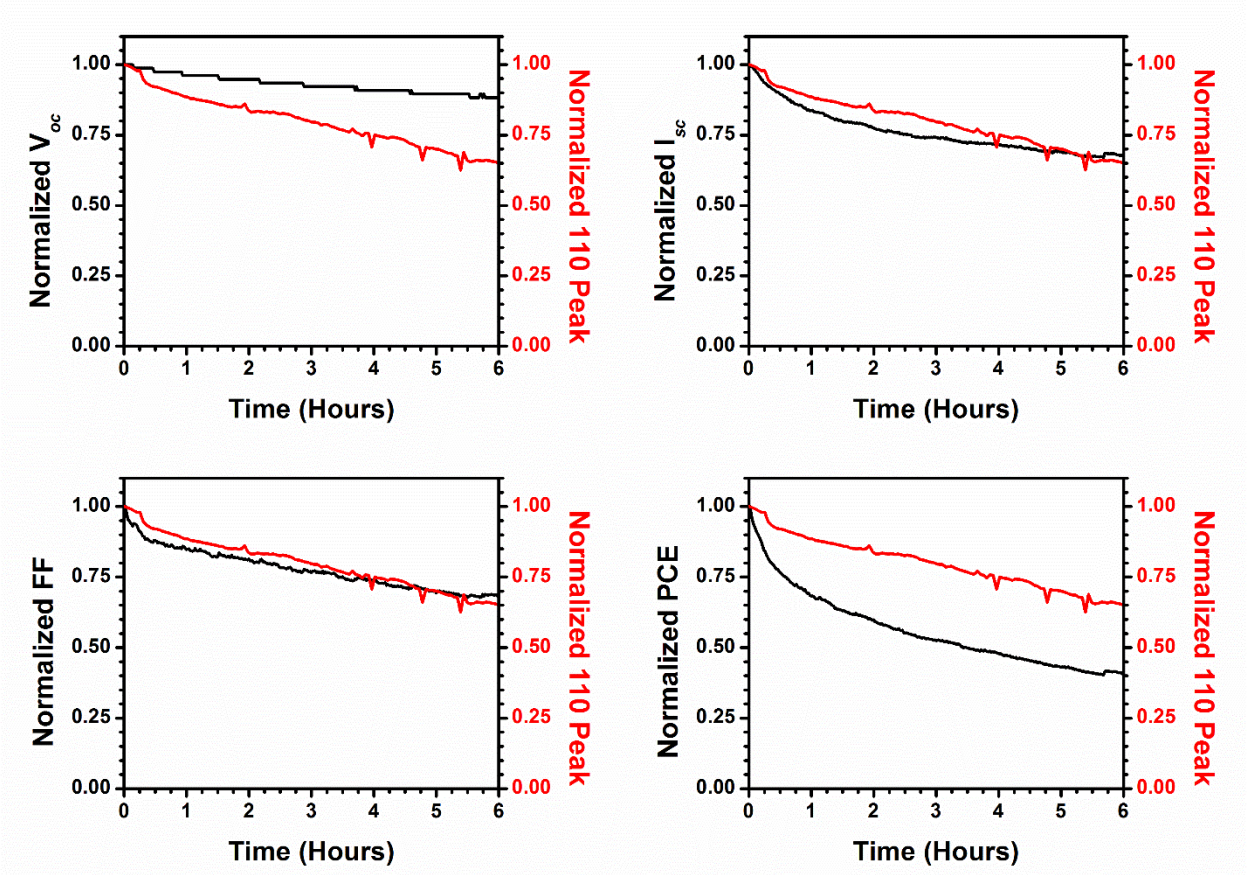

Figure 3.11 Combined GIWAXS and I-V data for gold electrode device in dry conditions.

3.3.2. Wet Conditions

Using a more stable gold electrode is expected to supress the electrode degradation observed at higher RH so that other humidity-driven effects become apparent. The starting GIWAXS pattern along with the initial I-V curve for the sample are shown in Figure 3.12. From the GIWAXS data the $MAPbI_3$ film did not undergo full conversion, and there is a substantial amount of latent lead iodide present, as shown by the peak present at 0.91 $Å^{-1}$. This is not expected to be problematic since having some residual lead iodide can actually be beneficial for device performance.[77,78]

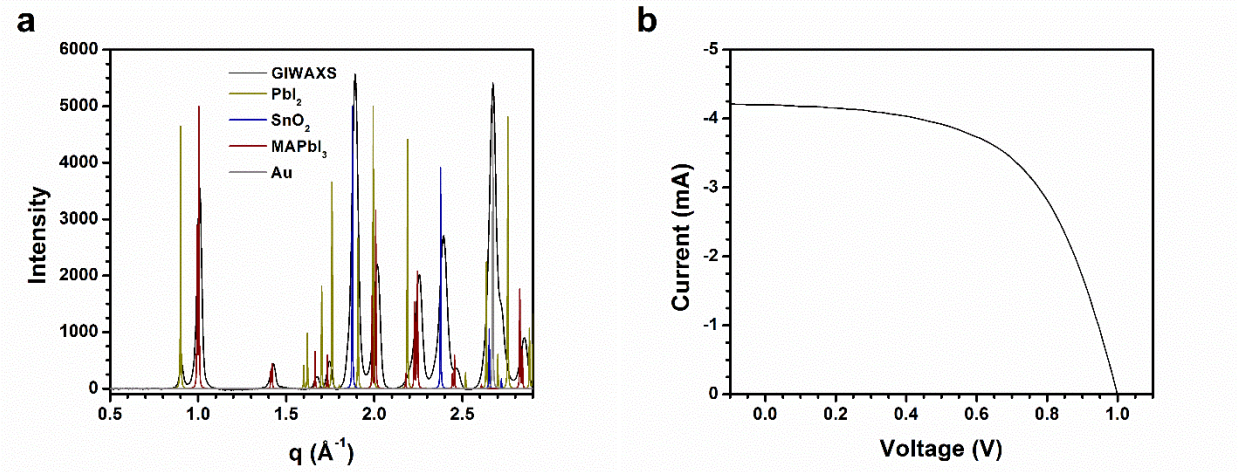

Figure 3.12 Initial GIWAXS scattering (right) and I-V curve (left) for wet gold devices.

The degradation experiment at high RH was performed in the same way as the others, with the time corelated GIWAXS data (Figure 3.13a) showing little change in the crystal structure over time. However, the I-V trend (Figure 3.13b) was very different compared to the silver data. As the device degrades a bump forms in the I-V curve. Previous work has shown that this bump is due to slow ion migration in the cell; this affects the effective potential in the cell, causing the artifact seen in the I-V curves.[76]

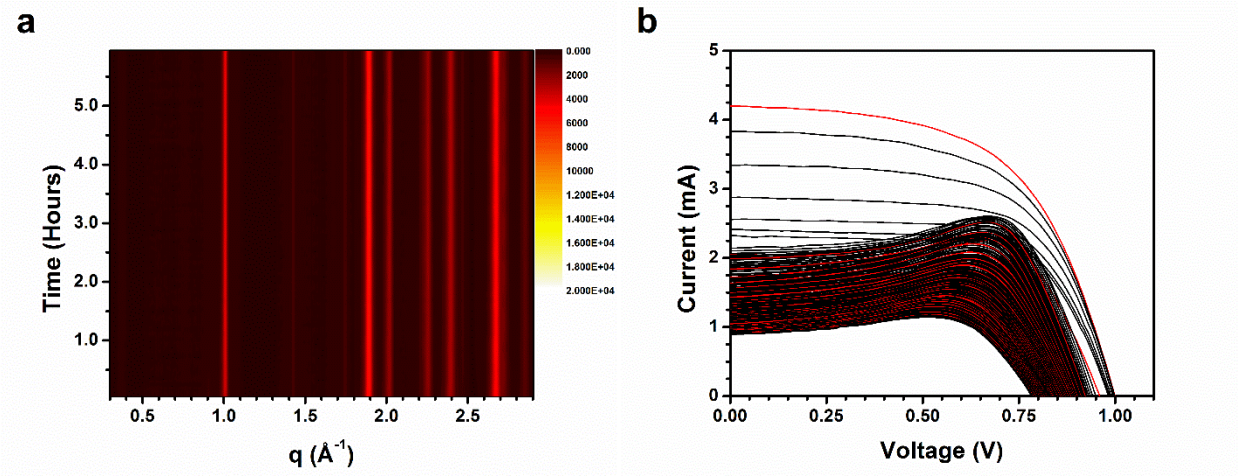

Figure 3.13 Time resolved data for: (a) GIWAXS data in a matrix plot and (b) I-V curve trend for device with gold electrode in ~85% RH.

The correlated data from this experiment is shown in Figure 3.14. When compared to the dry data, there is a faster initial drop in device current and efficiency. The device clearly degrades faster than the dry device. However, some unique features are present in the data that were not seen in the other experiments. The first is that there was an overall increase in the intensity of the (110) perovskite scattering peak. This can be attributed to the healing effects[59,79] that water can have on lead halide perovskites. As the water penetrates the active layer, the perovskite can partially dissolve at the grain boundaries and reform to make larger grains. Along with an increase in the intensity of the perovskite peaks there is a decrease in the intensity of the residual PbI_2 peak (Figure 3.15), that shows that there may be further conversion of PbI_2 into the perovskite material. This combined with the fact that small amount PbI_2 has been shown to be beneficial to solar cell performance,[77] there is further study in having a small amount unconverted from processing the films, compared to full conversion.

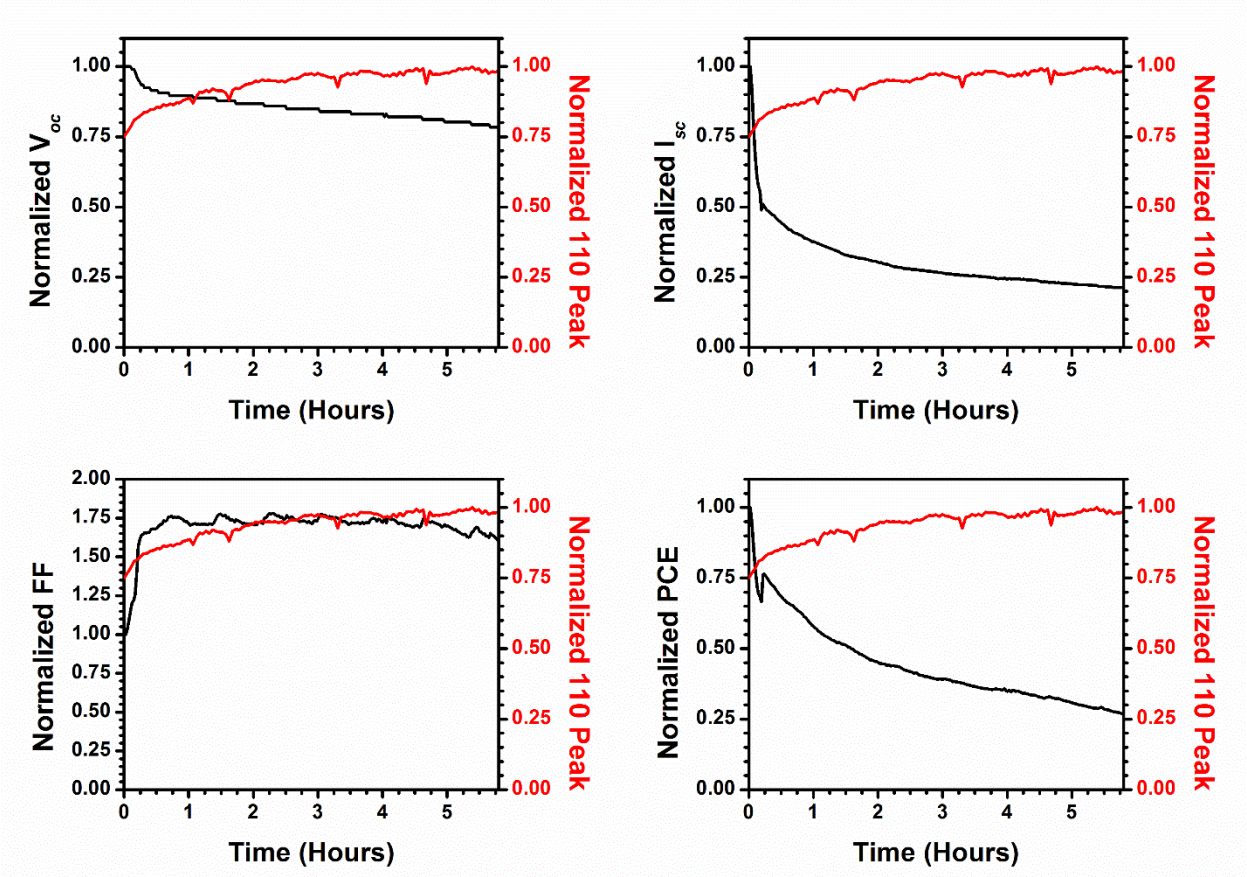

Figure 3.14 Correlated time resolved GIWAXS and I-V data for gold electrode device in ~ 85% RH conditions.

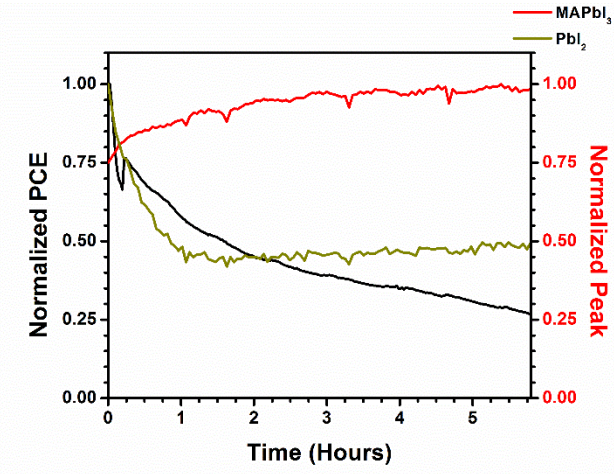

Figure 3.15 Plot of time correlated PCE, $MAPbI_3$, and residual PbI_2 trends.

The other major difference in the data is that there is a substantial increase in the fill factor over time. This increase is an artifact; as water penetrates the sample, there is a significant increase in the hysteresis of the device I-V curve. This causes the fill factor to become artificially inflated due to how it is calculated. The fill factor is calculated from the maximum power point (shown in Figure 3.16). This maximum power point gives a current higher than the I_{sc} which results in a larger fill factor than calculated from the y and x-intercepts. This increase in hysteresis is due to an increase in ion migration caused by the inclusion of water molecules in the perovskite layer. A previous study has shown that water can penetrate into $MAPbI_3$ without disrupting the crystal structure of the material,[80] and explains why the GIWAXS pattern remains unchanged during this process. As the iodide ions are slow moving they build up an internal charge in the device at slow scan rates.[76] As the charge build up dissipates, a localized increase in current output produces the bump in the I-V curve. This effect also accounts for the slight increases in device efficiency at around the 15 minute mark.

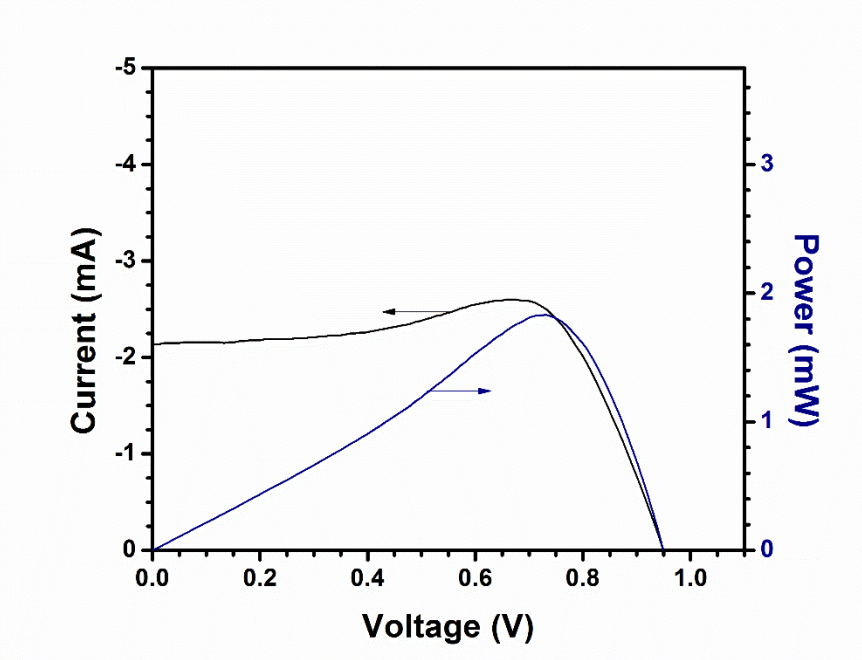

Figure 3.16 I-V curve of device (black line) with power output (blue line) after 15 minute exposure to high RH.

When the gold degradation data in Figure 3.14 is compared to the silver degradation data in Figure 3.7, a significant improvement in device lifetime can be seen. This can be attributed to the stability difference between gold and silver; PbI_2 impurity in the gold sample can improve the performance but is minor compared to the total lifetime. As gold is a more inert metal compared to silver, it can resist corrosion from iodide that is transported across the HTL of the device. From the observed bump in the I-V curves, ion migration still happens regardless of the electrode materials used. Even though the gold electrode is more resistant to iodide corrosion than silver, the general mechanism for loss of performance is the same. Ion migration in the device causes a decrease in charge carrier extraction efficiency resulting, in a loss of I_{sc} and PCE.

While ion migration is likely the major culprit of performance loss, other effects cannot be ruled out. One effect known to result from humidity conditioning is water partially dissolving and recrystalizing the perovskite.[79] This means that on the surface of some crystallites there is

both water and possibly dissolved perovskite. This could have the effect of increasing the number of trap states in the material and increasing series resistance. However, if these partially solvated grain boundaries interconnect, then there would also be an a decrease in the shunt resistance for the device, which would cause a performance loss. This effect due to the presence of surface moisture should be highly reversible, as the loss of water would reform the perovskite.

The other effect that could be happening is changes in the mechanical structure of the device. As the perovskite crystallinity changes there can be mechanical stress on the device interlayers. As mechanical strain increases, delamination of device layers is possible. This delamination causes the formation of gaps that increase the series resistance of the device, reducing overall performance.

What is apparent from the diffraction data in all four experiments is that there is no apparent formation of the hydrates previously observed at high humidity. The extended decomposition time of the gold devices was still not enough to see the presence of any hydrate peaks. This formation of hydrate phases is discussed further in section 3.4.

3.4 Cycling Illumination

One of the original goals of this thesis was to determine the effect that hydrates had on device performance over time. The hydrates form readily in experiments on thin films[68] at humidities comparable to those used in these experiments. However, the hydrates proved to be elusive in the *operando* experiments performed in this thesis. To determine why hydrates were not observed in the *operando* studies, an experiment was done where the lighting conditions were cycled. The sample was exposed to RH $\geq$ 90% with no illumination; 3 second X-ray exposures were taken until a large hydrate peak formed. The sample was then exposed to the light source; 0.5 second X-ray exposures were taken. Diffraction data is shown in Figure 3.17.

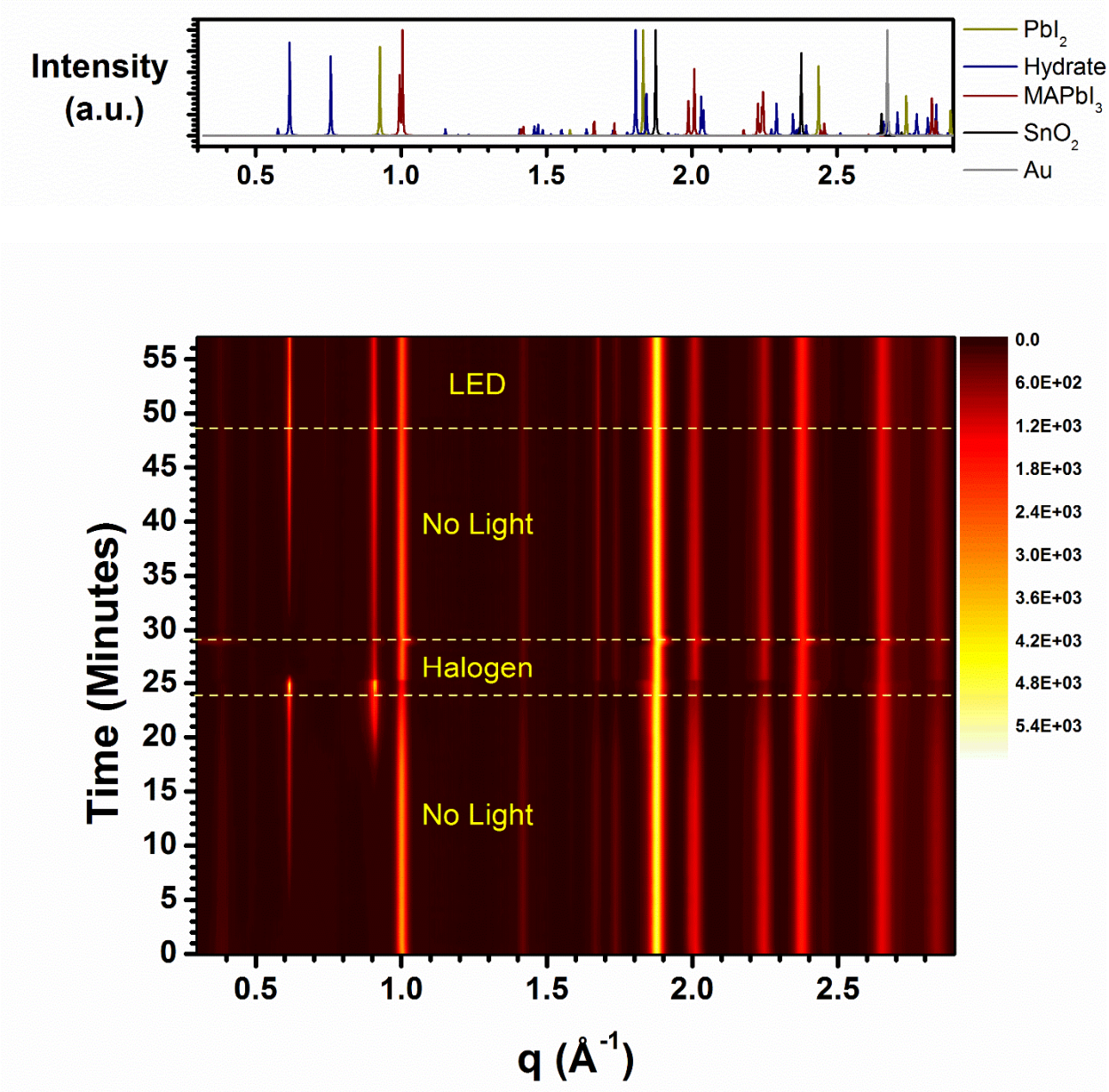

Figure 3.17 Light cycling of a gold perovskite device in high humidity with theoretical peak spectra.

The sample in the dark was subjected to a RH ≥ 90% and the appearance of hydrates was quickly apparent in the GIWAXS pattern. Once a sufficient amount of hydrates formed, the halogen lamp was turned on. The hydrates disappeared very quickly. Interestingly the PbI_2 peak ($q = 0.91$ Å^{-1}) also showed a significant decrease in intensity along with a quick increase in

perovskite intensity at the 25 minute mark. After some time, the light was turned off and the hydrates reformed. After a significant amount of hydrate reformed, a LED light source was used to illuminate the sample. No loss of hydrates was noticed in the GIWAXS pattern.

The output spectrum for each light source is shown in Figure 3.18. The halogen light source has a significantly more intense infrared component compared to the LED light source. This results in higher thermal loading of the sample compared to the LED. This suggests that the hydrates are unstable to the increase in temperature caused by the halogen lamp. Since there was no decrease in the intensity of the hydrate peaks on light exposure to the LED, the hydrate appears to be photochemically stable. The thermal decomposition of the hydrate may be driven by a reduction in the RH near the sample. This reduction in RH could lead to the desorption of water from the sample and a regeneration of the perovskite phase as small changes in RH can have large effect on the amount of water that the perovskite absorbs.[80]

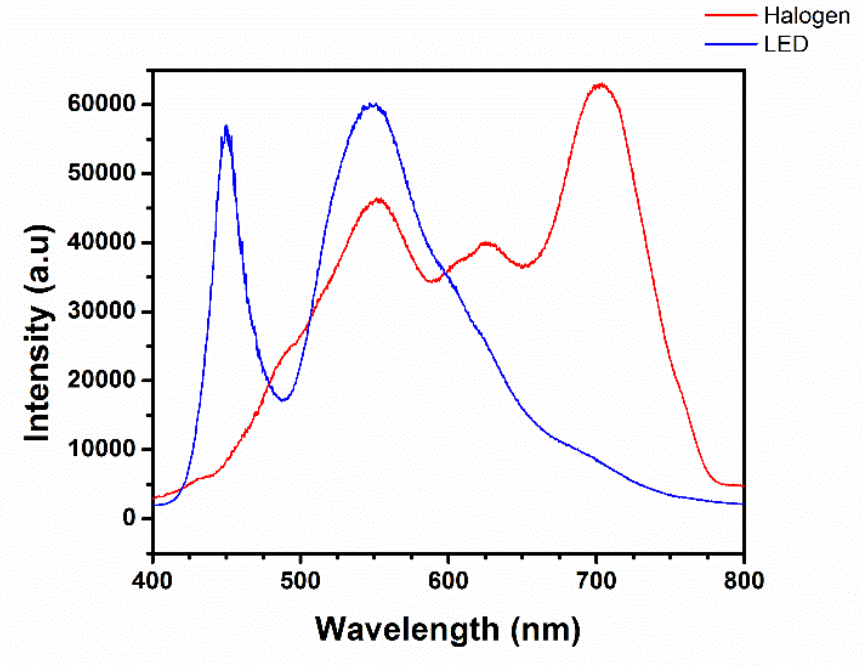

Figure 3.18 The spectral output for halogen and LED light source from 400-800 nm.

One final possibility is that hydrates are still present, but the thermal loading is causing them to become amorphous. Since GIWAXS is insensitive to amorphous material, it cannot be ruled out that moisture remains in the sample. There is evidence that water can penetrate into the crystal structure of the perovskite without changing the structure.[80] This means that it is possible that the increase in temperature either reduces the humidity enough to regenerate to the perovskite structure or the heat causes the structure to remain intact even with the water present.

These results mean that how these cells behave and degrade changes with the environment that they operate in. This environment changes during the day, as even the cycling of the sun through a 24 hour day presents two very different environments for the cell to degrade in. The AM1.5G[81] spectral distribution for the sun during the day (as shown in Figure 3.19) shows a large amount of energy in the infrared region that will vary throughout the day. Weather, climate, and seasonal effects changes will also affect how a cell degrades. This means that testing these devices for commercial applications will require many environmental variables to be studied. The use of *operando* experiments will be required to achieve a full understanding of how these cells will perform in reality. They will give a better picture of how perovskite solar cells degrade and how best to prevent it.

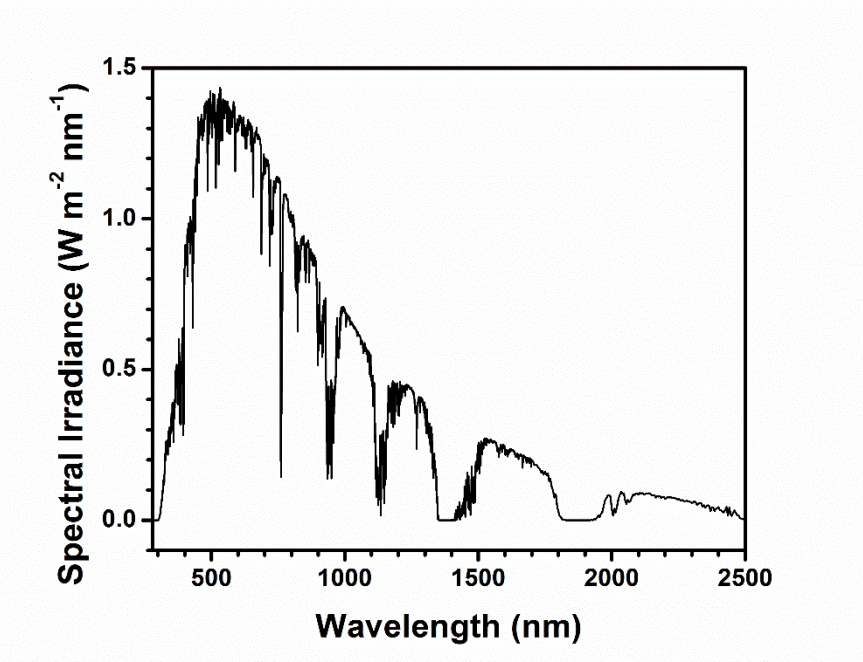

Figure 3.19 Spectral distribution at 48.18° tilt through the atmosphere (AM1.5G).

Chapter 4 Conclusion

4.1 Summary

In this thesis the original goal was to develop an experimental apparatus and protocol to test perovskite solar cells *operando* to gain a better understanding of how they degrade. The goal was also to gain a better understanding of how hydrate phases affect device performance. This testing was done using devices with either a gold or silver top electrode.

The devices with silver electrodes were used to test a known effect in literature where iodide ions migrate across the HTL of the device and react with silver electrode.[82] By testing a known phenomenon, the experimental setup could be tested to make sure that it worked properly. The main difference between what was expected from the literature and the experimental results was the lack of hydrate phases present in the active layer. The devices once exposed to moisture showed a rapid decrease in performance which was due to the formation of a silver iodide layer that led to an increase in the rate of recombination.

For the gold-based devices the metallic electrode is resistant to iodine attack and the devices had a longer lifetime compared to those with silver electrodes. What was seen in the electrical data was that the device had a significant increase in hysteresis as it was exposed to humidity. An increase in ion migration within the perovskite material led to a slow build up of charge in the gold devices leading to a significant increase in hysteresis. The device degradation showed a major loss in current, as apposed to the voltage. The loss in current is not due to material degradation, as the diffraction data shows an increase in perovskite crystallinity with

time. This is caused by moisture penetration into the device that can dissolve and recrystalize the perovskite at the grain boundaries.

The final experiment in this thesis shows that the hydrate phases are not stable under illumination by a halogen lamp due to heating of the sample. This causes the hydrates not to form, as observed in the diffraction data; however, it cannot be ruled out that they form in minute quantities. Since they may only form in minute quantities under operating conditions, they are unlikely to be a significant contributor to device degradation when compared to other effects.

Overall the field of perovskite solar cells is focused on improving the intrinsic stability of the perovskite material to improve lifetimes. The majority of testing done is through *ex situ* experiments which can miss important processes such as hydrate formation, since water ingress is a reversible process. The data in Chapter 3 shows that degradation of the active material is not the main factor behind the loss of performance in $MAPbI_3$ based devices. Instead electrode degradation, an increase in trap state density, and a reduction of shunt resistance are larger contributing factors to degradation. The results suggest that the surface passivation of perovskite grains may help prevent the problems caused by water ingress at high RH.

4.2 Future Work

The experimental test bed that was developed in this thesis can be expanded to multiple other devices and environments. In just the perovskite field there are future projects in just testing different formulations of perovskite that change the A site and B site ions. This will allow researchers to see how the composition affects the lifetime of devices and the main route of failure. Even with the devices used in this thesis there are projects to see how variation in the production of a cell affects the way it fails. While studying the effects of high RH in section 3.3.2 another device was put through the same experiment. The resulting correlated data (Figure

4.1) shows a different short-term trend of increasing PCE and perovskite (110) intensity, followed by a rapid decrease in performance, then a slow decay of both performance and perovskite peak intensity. The device failure mechanism could be affected by the film quality and the presence of impurities. A more in-depth study would need to be done to make the same perovskite devices using different techniques, such as one step perovskite formation[48,57] versus two step dip methods,[55] and devices made inside a glovebox versus in open atmosphere. This type of study would show whether the device fabrication process affects the device lifetime. Including in this is to test weather small amount of PbI_2 impurities improve device lifetimes.

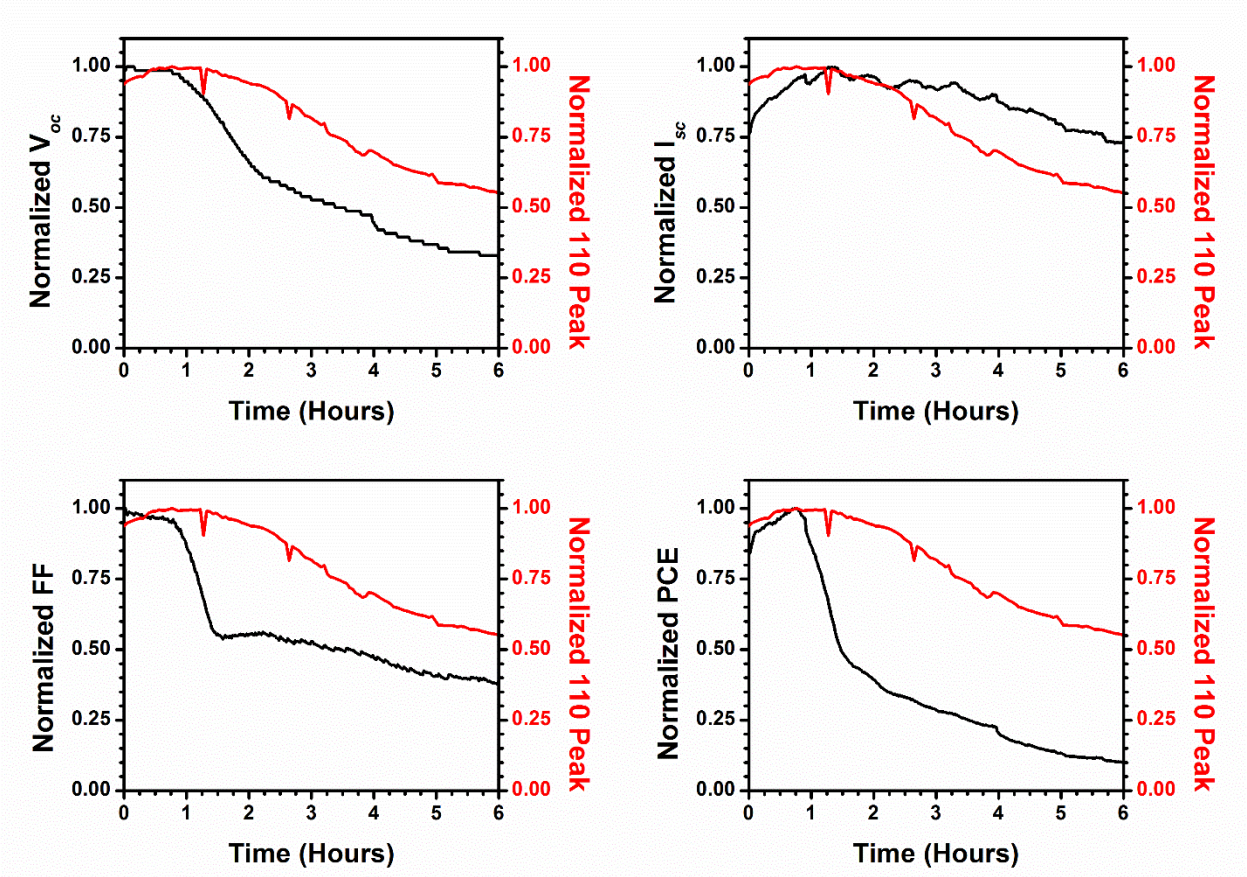

Figure 4.1 Second $MAPbI_3$ device with gold electrode exposed to +85% RH.

Other future work could investigate other environmental conditions, such as oxygen, humidity, heat, or a combination of all three. This would determine if there are different degradation pathways for perovskite devices depending on their environment and how the materials used in the devices affect the stability. These experiments would bring perovskite devices closer to real world application.

This test bench can be applied to any crystalline material that has a device structure similar to the one presented in this thesis. As such it could be used to test other thin film solar cell technologies in a variety of controlled environments to gather *operando* data. This type of *operando* data will be important to many new solar technologies as a way determine how to best optimize devices for commercialization.

Chapter 5 References

(1) Newman, T. P. Tracking the Release of IPCC AR5 on Twitter: Users, Comments, and Sources Following the Release of the Working Group I Summary for Policymakers. *Public Underst. Sci.* **2017**, *26*, 815–825.

(2) Bruckner, T.; Bashmakov, I. A.; Mulugetta, Y.; Chum, H.; de la Vega Navarro, A.; Edmonds, J.; Faaij, A.; Fungtammasan, B.; Garg, A.; Hertwich, E.; et al. Energy Systems. In *Climate Change 2014: Mitigation of Climate Change. Contribution of Working Group III to the Fifth Assessment Report of the Intergovernmental Panel on Climate Change [Edenhofer, O., R. Pichs-Madruga, Y. Sokona, E. Farahani, S. Kadner, K. Seyboth, A. Adler, I. Baum, S. Brunner, P. Eickemeier, B. Kriemann, J. Savolainen, S. Schlömer, C. von Stechow, T. Zwickel and J.C. Minx (eds.)]. Cambridge University Press, Cambridge, United Kingdom and New York, NY, USA.*; 2014.

(3) *World Energy Outlook*; International Energy Agency, 2017.

(4) NREL https://www.nrel.gov/pv/assets/images/efficiency-chart.png (accessed May 18, 2018).

(5) Shockley, W.; Queisser, H. J. Detailed Balance Limit of Efficiency of P-n Junction Solar Cells. *J. Appl. Phys.* **1961**, *32*, 510–519.

(6) Rühle, S. Tabulated Values of the Shockley–Queisser Limit for Single Junction Solar Cells. *Sol. Energy* **2016**, *130*, 139–147.

(7) NREL efficiency chart http://www.nrel.gov/ncpv/images/ e ffi ciency_chart.jpg.

(8) Yusoff, A. R. bin M.; Kim, D.; Kim, H. P.; Shneider, F. K.; da Silva, W. J.; Jang, J. A High Efficiency Solution Processed Polymer Inverted Triple-Junction Solar Cell Exhibiting a Power Conversion Efficiency of 11.83%. *Energy Environ. Sci.* **2015**, *8*, 303–316.

(9) Mailoa, J. P.; Bailie, C. D.; Johlin, E. C.; Hoke, E. T.; Akey, A. J.; Nguyen, W. H.; McGehee, M. D.; Buonassisi, T. A 2-Terminal Perovskite/silicon Multijunction Solar Cell Enabled by a Silicon Tunnel Junction. *Appl. Phys. Lett.* **2015**, *106*, 121105.

(10) Yamaguchi, M.; Nishimura, K.-I.; Sasaki, T.; Suzuki, H.; Arafune, K.; Kojima, N.; Ohsita, Y.; Okada, Y.; Yamamoto, A.; Takamoto, T.; et al. Novel Materials for High-Efficiency III–V Multi-Junction Solar Cells. *Sol. Energy* **2008**, *82*, 173–180.

(11) Bailie, C. D.; Christoforo, M. G.; Mailoa, J. P.; Bowring, A. R.; Unger, E. L.; Nguyen, W. H.; Burschka, J.; Pellet, N.; Lee, J. Z.; Gratzel, M.; et al. Semi-Transparent Perovskite Solar Cells for Tandems with Silicon and CIGS. *Energy Environ. Sci.* **2015**, *8*, 956–963.

(12) Yamaguchi, M.; Takamoto, T.; Araki, K. Super High-Efficiency Multi-Junction and Concentrator Solar Cells. *14th Int. Photovolt. Sci. Eng. Conf.* **2006**, *90*, 3068–3077.

(13) Dimroth, F.; Grave, M.; Beutel, P.; Fiedeler, U.; Karcher, C.; Tibbits, T. N. D.; Oliva, E.; Siefer, G.; Schachtner, M.; Wekkeli, A.; et al. Wafer Bonded Four-Junction GaInP/GaAs//GaInAsP/GaInAs Concentrator Solar Cells with 44.7% Efficiency. *Prog. Photovolt. Res. Appl.* **2014**, *22*, 277–282.

(14) Kranz, L.; Gretener, C.; Perrenoud, J.; Schmitt, R.; Pianezzi, F.; La Mattina, F.; Blösch, P.; Cheah, E.; Chirilă, A.; Fella, C. M.; et al. Doping of Polycrystalline CdTe for High-Efficiency Solar Cells on Flexible Metal Foil. *Nat. Commun.* **2013**, *4*, 2306.

(15) Kaelin, M.; Rudmann, D.; Tiwari, A. N. Low Cost Processing of CIGS Thin Film Solar Cells. *Thin Film PV* **2004**, *77*, 749–756.
(16) Hwang, K.; Jung, Y.-S.; Heo, Y.-J.; Scholes, F. H.; Watkins, S. E.; Subbiah, J.; Jones, D. J.; Kim, D.-Y.; Vak, D. Toward Large Scale Roll-to-Roll Production of Fully Printed Perovskite Solar Cells. *Adv. Mater.* **2015**, *27*, 1241–1247.
(17) Krebs, F. C.; Tromholt, T.; Jorgensen, M. Upscaling of Polymer Solar Cell Fabrication Using Full Roll-to-Roll Processing. *Nanoscale* **2010**, *2*, 873–886.
(18) Krebs, F. C.; Fyenbo, J.; Jorgensen, M. Product Integration of Compact Roll-to-Roll Processed Polymer Solar Cell Modules: Methods and Manufacture Using Flexographic Printing, Slot-Die Coating and Rotary Screen Printing. *J. Mater. Chem.* **2010**, *20*, 8994–9001.
(19) Holliday, S.; Ashraf, R. S.; Wadsworth, A.; Baran, D.; Yousaf, S. A.; Nielsen, C. B.; Tan, C.-H.; Dimitrov, S. D.; Shang, Z.; Gasparini, N.; et al. High-Efficiency and Air-Stable P3HT-Based Polymer Solar Cells with a New Non-Fullerene Acceptor. *Nat. Commun.* **2016**, *7*, 11585.
(20) Lin, Y.; Zhao, F.; He, Q.; Huo, L.; Wu, Y.; Parker, T. C.; Ma, W.; Sun, Y.; Wang, C.; Zhu, D.; et al. High-Performance Electron Acceptor with Thienyl Side Chains for Organic Photovoltaics. *J. Am. Chem. Soc.* **2016**, *138*, 4955–4961.
(21) Pan, Z.; Mora-Seró, I.; Shen, Q.; Zhang, H.; Li, Y.; Zhao, K.; Wang, J.; Zhong, X.; Bisquert, J. High-Efficiency "Green" Quantum Dot Solar Cells. *J. Am. Chem. Soc.* **2014**, *136*, 9203–9210.
(22) Zhang, J.; Gao, J.; Church, C. P.; Miller, E. M.; Luther, J. M.; Klimov, V. I.; Beard, M. C. PbSe Quantum Dot Solar Cells with More than 6% Efficiency Fabricated in Ambient Atmosphere. *Nano Lett.* **2014**, *14*, 6010–6015.
(23) Du, J.; Du, Z.; Hu, J.-S.; Pan, Z.; Shen, Q.; Sun, J.; Long, D.; Dong, H.; Sun, L.; Zhong, X.; et al. Zn–Cu–In–Se Quantum Dot Solar Cells with a Certified Power Conversion Efficiency of 11.6%. *J. Am. Chem. Soc.* **2016**, *138*, 4201–4209.
(24) Im, J.-H.; Lee, C.-R.; Lee, J.-W.; Park, S.-W.; Park, N.-G. 6.5% Efficient Perovskite Quantum-Dot-Sensitized Solar Cell. *Nanoscale* **2011**, *3*, 4088–4093.
(25) Roldan-Carmona, C.; Gratia, P.; Zimmermann, I.; Grancini, G.; Gao, P.; Graetzel, M.; Nazeeruddin, M. K. High Efficiency Methylammonium Lead Triiodide Perovskite Solar Cells: The Relevance of Non-Stoichiometric Precursors. *Energy Environ. Sci.* **2015**, *8*, 3550–3556.
(26) Bi, D.; Yi, C.; Luo, J.; Décoppet, J.-D.; Zhang, F.; Zakeeruddin, S. M.; Li, X.; Hagfeldt, A.; Grätzel, M. Polymer-Templated Nucleation and Crystal Growth of Perovskite Films for Solar Cells with Efficiency Greater than 21%. *Nat. Energy* **2016**, *1*, 16142.
(27) Kojima, A.; Teshima, K.; Shirai, Y.; Miyasaka, T. Organometal Halide Perovskites as Visible-Light Sensitizers for Photovoltaic Cells. *J. Am. Chem. Soc.* **2009**, *131*, 6050–6051.
(28) Yang, W. S.; Park, B.-W.; Jung, E. H.; Jeon, N. J.; Kim, Y. C.; Lee, D. U.; Shin, S. S.; Seo, J.; Kim, E. K.; Noh, J. H.; et al. Iodide Management in Formamidinium-Lead-Halide–based Perovskite Layers for Efficient Solar Cells. *Science* **2017**, *356*, 1376.
(29) Hao, F.; Stoumpos, C. C.; Cao, D. H.; Chang, R. P. H.; Kanatzidis, M. G. Lead-Free Solid-State Organic–inorganic Halide Perovskite Solar Cells. *Nat. Photonics* **2014**, *8*, 489.
(30) Kulbak, M.; Gupta, S.; Kedem, N.; Levine, I.; Bendikov, T.; Hodes, G.; Cahen, D. Cesium Enhances Long-Term Stability of Lead Bromide Perovskite-Based Solar Cells. *J. Phys. Chem. Lett.* **2016**, *7*, 167–172.

(31) Edri, E.; Kirmayer, S.; Kulbak, M.; Hodes, G.; Cahen, D. Chloride Inclusion and Hole Transport Material Doping to Improve Methyl Ammonium Lead Bromide Perovskite-Based High Open-Circuit Voltage Solar Cells. *J. Phys. Chem. Lett.* **2014**, *5*, 429–433.
(32) Ahn, N.; Son, D.-Y.; Jang, I.-H.; Kang, S. M.; Choi, M.; Park, N.-G. Highly Reproducible Perovskite Solar Cells with Average Efficiency of 18.3% and Best Efficiency of 19.7% Fabricated via Lewis Base Adduct of Lead(II) Iodide. *J. Am. Chem. Soc.* **2015**, *137*, 8696–8699.
(33) Suarez, B.; Gonzalez-Pedro, V.; Ripolles, T. S.; Sanchez, R. S.; Otero, L.; Mora-Sero, I. Recombination Study of Combined Halides (Cl, Br, I) Perovskite Solar Cells. *J. Phys. Chem. Lett.* **2014**, *5*, 1628–1635.
(34) You, J.; Hong, Z.; Yang, Y. (Michael); Chen, Q.; Cai, M.; Song, T.-B.; Chen, C.-C.; Lu, S.; Liu, Y.; Zhou, H.; et al. Low-Temperature Solution-Processed Perovskite Solar Cells with High Efficiency and Flexibility. *ACS Nano* **2014**, *8*, 1674–1680.
(35) Liu, D.; Kelly, T. L. Perovskite Solar Cells with a Planar Heterojunction Structure Prepared Using Room-Temperature Solution Processing Techniques. *Nat Photon* **2014**, *8*, 133–138.
(36) Poorkazem, K.; Liu, D.; Kelly, T. L. Fatigue Resistance of a Flexible, Efficient, and Metal Oxide-Free Perovskite Solar Cell. *J. Mater. Chem. A* **2015**, *3*, 9241–9248.
(37) Kim, B. J.; Kim, D. H.; Lee, Y.-Y.; Shin, H.-W.; Han, G. S.; Hong, J. S.; Mahmood, K.; Ahn, T. K.; Joo, Y.-C.; Hong, K. S.; et al. Highly Efficient and Bending Durable Perovskite Solar Cells: Toward a Wearable Power Source. *Energy Environ. Sci.* **2015**, *8*, 916–921.
(38) Rossander, L. H.; Larsen-Olsen, T. T.; Dam, H. F.; Schmidt, T. M.; Corazza, M.; Norrman, K.; Rajkovic, I.; Andreasen, J. W.; Krebs, F. C. In Situ X-Ray Scattering of Perovskite Solar Cell Active Layers Roll-to-Roll Coated on Flexible Substrates. *CrystEngComm* **2016**, *18*, 5083–5088.
(39) Wei, Z.; Chen, H.; Yan, K.; Yang, S. Inkjet Printing and Instant Chemical Transformation of a CH3NH3PbI3/Nanocarbon Electrode and Interface for Planar Perovskite Solar Cells. *Angew. Chem. Int. Ed.* **2014**, *53*, 13239–13243.
(40) Yang, J.; Kelly, T. L. Decomposition and Cell Failure Mechanisms in Lead Halide Perovskite Solar Cells. *Inorg. Chem.* **2016**.
(41) Yang, J.; Siempelkamp, B. D.; Mosconi, E.; De Angelis, F.; Kelly, T. L. Origin of the Thermal Instability in CH3NH3PbI3 Thin Films Deposited on ZnO. *Chem. Mater.* **2015**, *27*, 4229–4236.
(42) Bryant, D.; Aristidou, N.; Pont, S.; Sanchez-Molina, I.; Chotchunangatchaval, T.; Wheeler, S.; Durrant, J. R.; Haque, S. A. Light and Oxygen Induced Degradation Limits the Operational Stability of Methylammonium Lead Triiodide Perovskite Solar Cells. *Energy Environ. Sci.* **2016**, *9*, 1655–1660.
(43) Misra, R. K.; Aharon, S.; Li, B.; Mogilyansky, D.; Visoly-Fisher, I.; Etgar, L.; Katz, E. A. Temperature- and Component-Dependent Degradation of Perovskite Photovoltaic Materials under Concentrated Sunlight. *J. Phys. Chem. Lett.* **2015**, *6*, 326–330.
(44) Song, Z.; Abate, A.; Watthage, S. C.; Liyanage, G. K.; Phillips, A. B.; Steiner, U.; Graetzel, M.; Heben, M. J. Perovskite Solar Cell Stability in Humid Air: Partially Reversible Phase Transitions in the PbI2-CH3NH3I-H2O System. *Adv. Energy Mater.* **2016**, 1600846–n/a.

(45) Miyata, A.; Mitioglu, A.; Plochocka, P.; Portugall, O.; Wang, J. T.-W.; Stranks, S. D.; Snaith, H. J.; Nicholas, R. J. Direct Measurement of the Exciton Binding Energy and Effective Masses for Charge Carriers in Organic–inorganic Tri-Halide Perovskites. *Nat. Phys.* **2015**, *11*, 582.
(46) D'Innocenzo, V.; Grancini, G.; Alcocer, M. J. P.; Kandada, A. R. S.; Stranks, S. D.; Lee, M. M.; Lanzani, G.; Snaith, H. J.; Petrozza, A. Excitons versus Free Charges in Organo-Lead Tri-Halide Perovskites. *Nat. Commun.* **2014**, *5*, 3586.
(47) Lee, M. M.; Teuscher, J.; Miyasaka, T.; Murakami, T. N.; Snaith, H. J. Efficient Hybrid Solar Cells Based on Meso-Superstructured Organometal Halide Perovskites. *Science* **2012**, *338*, 643.
(48) Liu, M.; Johnston, M. B.; Snaith, H. J. Efficient Planar Heterojunction Perovskite Solar Cells by Vapour Deposition. *Nature* **2013**, *501*, 395.
(49) Eperon, G. E.; Stranks, S. D.; Menelaou, C.; Johnston, M. B.; Herz, L. M.; Snaith, H. J. Formamidinium Lead Trihalide: A Broadly Tunable Perovskite for Efficient Planar Heterojunction Solar Cells. *Energy Environ. Sci.* **2014**, *7*, 982–988.
(50) Clegg, C.; Hill, I. G. Systematic Study on the Impact of Water on the Performance and Stability of Perovskite Solar Cells. *RSC Adv.* **2016**, *6*, 52448–52458.
(51) Leguy, A. M. A.; Hu, Y.; Campoy-Quiles, M.; Alonso, M. I.; Weber, O. J.; Azarhoosh, P.; van Schilfgaarde, M.; Weller, M. T.; Bein, T.; Nelson, J.; et al. Reversible Hydration of CH3NH3PbI3 in Films, Single Crystals, and Solar Cells. *Chem. Mater.* **2015**, *27*, 3397–3407.
(52) Divitini, G.; Cacovich, S.; Matteocci, F.; Cinà, L.; Di Carlo, A.; Ducati, C. In Situ Observation of Heat-Induced Degradation of Perovskite Solar Cells. *Nat. Energy* **2016**, *1*, 15012.
(53) Yang, J.; Fransishyn, K. M.; Kelly, T. L. Comparing the Effect of Mesoporous and Planar Metal Oxides on the Stability of Methylammonium Lead Iodide Thin Films. *Chem. Mater.* **2016**, *28*, 7344–7352.
(54) Filip, M. R.; Eperon, G. E.; Snaith, H. J.; Giustino, F. Steric Engineering of Metal-Halide Perovskites with Tunable Optical Band Gaps. *Nat. Commun.* **2014**, *5*, 5757.
(55) Kulkarni, S. A.; Baikie, T.; Boix, P. P.; Yantara, N.; Mathews, N.; Mhaisalkar, S. Band-Gap Tuning of Lead Halide Perovskites Using a Sequential Deposition Process. *J. Mater. Chem. A* **2014**, *2*, 9221–9225.
(56) McMeekin, D. P.; Sadoughi, G.; Rehman, W.; Eperon, G. E.; Saliba, M.; Hörantner, M. T.; Haghighirad, A.; Sakai, N.; Korte, L.; Rech, B.; et al. A Mixed-Cation Lead Mixed-Halide Perovskite Absorber for Tandem Solar Cells. *Science* **2016**, *351*, 151.
(57) Saliba, M.; Matsui, T.; Seo, J.-Y.; Domanski, K.; Correa-Baena, J.-P.; Nazeeruddin, M. K.; Zakeeruddin, S. M.; Tress, W.; Abate, A.; Hagfeldt, A.; et al. Cesium-Containing Triple Cation Perovskite Solar Cells: Improved Stability, Reproducibility and High Efficiency. *Energy Environ. Sci.* **2016**, *9*, 1989–1997.
(58) Shirayama, M.; Kato, M.; Miyadera, T.; Sugita, T.; Fujiseki, T.; Hara, S.; Kadowaki, H.; Murata, D.; Chikamatsu, M.; Fujiwara, H. Degradation Mechanism of CH3NH3PbI3 Perovskite Materials upon Exposure to Humid Air. *J. Appl. Phys.* **2016**, *119*, 115501.
(59) Zhou, W.; Zhao, Y.; Shi, C.; Huang, H.; Wei, J.; Fu, R.; Liu, K.; Yu, D.; Zhao, Q. Reversible Healing Effect of Water Molecules on Fully Crystallized Metal–Halide Perovskite Film. *J. Phys. Chem. C* **2016**, *120*, 4759–4765.

(60) Nenon, D. P.; Christians, J. A.; Wheeler, L. M.; Blackburn, J. L.; Sanehira, E. M.; Dou, B.; Olsen, M. L.; Zhu, K.; Berry, J. J.; Luther, J. M. Structural and Chemical Evolution of Methylammonium Lead Halide Perovskites during Thermal Processing from Solution. *Energy Environ. Sci.* **2016**, *9*, 2072–2082.
(61) Habisreutinger, S. N.; Leijtens, T.; Eperon, G. E.; Stranks, S. D.; Nicholas, R. J.; Snaith, H. J. Carbon Nanotube/Polymer Composites as a Highly Stable Hole Collection Layer in Perovskite Solar Cells. *Nano Lett.* **2014**, *14*, 5561–5568.
(62) Philippe, B.; Park, B.-W.; Lindblad, R.; Oscarsson, J.; Ahmadi, S.; Johansson, E. M. J.; Rensmo, H. Chemical and Electronic Structure Characterization of Lead Halide Perovskites and Stability Behavior under Different Exposures—A Photoelectron Spectroscopy Investigation. *Chem. Mater.* **2015**, *27*, 1720–1731.
(63) Moore, D. T.; Sai, H.; Tan, K. W.; Smilgies, D.-M.; Zhang, W.; Snaith, H. J.; Wiesner, U.; Estroff, L. A. Crystallization Kinetics of Organic–Inorganic Trihalide Perovskites and the Role of the Lead Anion in Crystal Growth. *J. Am. Chem. Soc.* **2015**, *137*, 2350–2358.
(64) Aristidou Nicholas; Sanchez-Molina Irene; Chotchuangchutchaval Thana; Brown Michael; Martinez Luis; Rath Thomas; Haque Saif A. The Role of Oxygen in the Degradation of Methylammonium Lead Trihalide Perovskite Photoactive Layers. *Angew. Chem. Int. Ed.* **2015**, *54*, 8208–8212.
(65) Li, C.; Tscheuschner, S.; Paulus, F.; Hopkinson, P. E.; Kießling, J.; Köhler, A.; Vaynzof, Y.; Huettner, S. Iodine Migration and Its Effect on Hysteresis in Perovskite Solar Cells. *Adv. Mater.* **2016**, *28*, 2446–2454.
(66) Yuan, Y.; Huang, J. Ion Migration in Organometal Trihalide Perovskite and Its Impact on Photovoltaic Efficiency and Stability. *Acc. Chem. Res.* **2016**, *49*, 286–293.
(67) Zhang, T.; Chen, H.; Bai, Y.; Xiao, S.; Zhu, L.; Hu, C.; Xue, Q.; Yang, S. Understanding the Relationship between Ion Migration and the Anomalous Hysteresis in High-Efficiency Perovskite Solar Cells: A Fresh Perspective from Halide Substitution. *Nano Energy* **2016**, *26*, 620–630.
(68) Yang, J.; Siempelkamp, B. D.; Liu, D.; Kelly, T. L. Investigation of CH3NH3PbI3 Degradation Rates and Mechanisms in Controlled Humidity Environments Using in Situ Techniques. *ACS Nano* **2015**, *9*, 1955–1963.
(69) Vincent, B. R.; Robertson, K. N.; Cameron, T. S.; Knop, O. Alkylammonium Lead Halides. Part 1. Isolated PbI64− Ions in (CH3NH3)4PbI6•2H2O. *Can. J. Chem.* **1987**, *65*, 1042–1046.
(70) Hao, F.; Stoumpos, C. C.; Liu, Z.; Chang, R. P. H.; Kanatzidis, M. G. Controllable Perovskite Crystallization at a Gas–Solid Interface for Hole Conductor-Free Solar Cells with Steady Power Conversion Efficiency over 10%. *J. Am. Chem. Soc.* **2014**, *136*, 16411–16419.
(71) Stoumpos, C. C.; Malliakas, C. D.; Kanatzidis, M. G. Semiconducting Tin and Lead Iodide Perovskites with Organic Cations: Phase Transitions, High Mobilities, and Near-Infrared Photoluminescent Properties. *Inorg. Chem.* **2013**, *52*, 9019–9038.
(72) Tan, K. W.; Moore, D. T.; Saliba, M.; Sai, H.; Estroff, L. A.; Hanrath, T.; Snaith, H. J.; Wiesner, U. Thermally Induced Structural Evolution and Performance of Mesoporous Block Copolymer-Directed Alumina Perovskite Solar Cells. *ACS Nano* **2014**, *8*, 4730–4739.
(73) Saliba, M.; Tan, K. W.; Sai, H.; Moore, D. T.; Scott, T.; Zhang, W.; Estroff, L. A.; Wiesner, U.; Snaith, H. J. Influence of Thermal Processing Protocol upon the

Crystallization and Photovoltaic Performance of Organic–Inorganic Lead Trihalide Perovskites. *J. Phys. Chem. C* **2014**, *118*, 17171–17177.
(74) Arora, N.; Dar, M. I.; Hinderhofer, A.; Pellet, N.; Schreiber, F.; Zakeeruddin, S. M.; Grätzel, M. Perovskite Solar Cells with CuSCN Hole Extraction Layers Yield Stabilized Efficiencies Greater than 20%. *Science* **2017**.
(75) Kimball Physics https://www.kimballphysics.com/shop/multi-cf-hardware/mcf450-sphcube-e6a8 (accessed May 18, 2018).
(76) Tress, W.; Marinova, N.; Moehl, T.; Zakeeruddin, S. M.; Nazeeruddin, M. K.; Gratzel, M. Understanding the Rate-Dependent J-V Hysteresis, Slow Time Component, and Aging in CH3NH3PbI3 Perovskite Solar Cells: The Role of a Compensated Electric Field. *Energy Environ. Sci.* **2015**, *8*, 995–1004.
(77) Kim, Y. C.; Jeon, N. J.; Noh, J. H.; Yang, W. S.; Seo, J.; Yun, J. S.; Ho-Baillie, A.; Huang, S.; Green, M. A.; Seidel, J.; et al. Beneficial Effects of PbI2 Incorporated in Organo-Lead Halide Perovskite Solar Cells. *Adv. Energy Mater.* **2016**, *6*, 1502104–n/a.
(78) Liu, F.; Dong, Q.; Wong, M. K.; Djurišić, A. B.; Ng, A.; Ren, Z.; Shen, Q.; Surya, C.; Chan, W. K.; Wang, J.; et al. Is Excess PbI2 Beneficial for Perovskite Solar Cell Performance? *Adv. Energy Mater.* **2016**, *6*, 1502206–n/a.
(79) Gangishetty, M. K.; Scott, R. W. J.; Kelly, T. L. Effect of Relative Humidity on Crystal Growth, Device Performance and Hysteresis in Planar Heterojunction Perovskite Solar Cells. *Nanoscale* **2016**, *8*, 6300–6307.
(80) Zhu, Z.; Hadjiev, V. G.; Rong, Y.; Guo, R.; Cao, B.; Tang, Z.; Qin, F.; Li, Y.; Wang, Y.; Hao, F.; et al. Interaction of Organic Cation with Water Molecule in Perovskite MAPbI3: From Dynamic Orientational Disorder to Hydrogen Bonding. *Chem. Mater.* **2016**, *28*, 7385–7393.
(81) Gueymard, C. A.; Myers, D.; Emery, K. Proposed Reference Irradiance Spectra for Solar Energy Systems Testing. *Sol. Energy* **2002**, *73*, 443–467.
(82) Kato, Y.; Ono, L. K.; Lee, M. V.; Wang, S.; Raga, S. R.; Qi, Y. Silver Iodide Formation in Methyl Ammonium Lead Iodide Perovskite Solar Cells with Silver Top Electrodes. *Adv. Mater. Interfaces* **2015**, *2*, 1500195–n/a.